IEEE Access
Multidisciplinary | Rapid Review | Open Access Journal

Received 22 December 2022, accepted 26 January 2023, date of publication 10 February 2023, date of current version 24 February 2023.

Digital Object Identifier 10.1109/ACCESS.2023.3244063

RESEARCH ARTICLE

Fourier-Optics Based Opto-Electronic Architectures for Simultaneous Multi-Band, Multi-Beam, and Wideband Transmit and Receive Phased Arrays

DENNIS W. PRATHER[1,2], (Fellow, IEEE), STEFANO GALLI[3], (Fellow, IEEE), GARRETT J. SCHNEIDER[1,2], SHOUYUAN SHI[1,2], JANUSZ A. MURAKOWSKI[2], (Member, IEEE), XIAO-FENG QI[1,2], (Senior Member, IEEE), AND CHRISTOPHER SCHUETZ[2]

[1]Department of Electrical and Computer Engineering, University of Delaware, Newark, DE 19716, USA
[2]Phase Sensitive Innovations, Inc., Newark, DE 19713, USA
[3]Peraton Laboratories, Wireless and Optical Department, Red Bank, NJ 07701, USA

Corresponding author: Dennis W. Prather (dprather@udel.edu)

This work was supported in part by the Air Force Office of Scientific Research (AFOSR), in part by the Office of Naval Research (ONR), and in part by the Air Force Research Laboratory (AFRL).

ABSTRACT Current trends in wireless communications require a Base Transceiver Station (BTS) to support an ever-increasing number of antennas, wider bandwidths, multiple frequency bands, and many simultaneous beams. This is a tall order when considering all-electronic implementations, especially when operating at high carrier frequencies. We describe here Fourier-optics based opto-electronic architectures that include analog and fully connected transmit (TX) and receive (RX) implementations that support simultaneous multi-band, multi-beam phased arrays wherein optical up- and down-conversion are used, respectively, to generate IF/RF and RF/IF signals for simultaneous multi-user and multi-beam transmission and reception over a wide range of frequencies. The proposed lens-based architectures have the ability to transmit and receive multiple distinct beams simultaneously even when only analog beamforming is performed, thus greatly simplifying the tasks of cell search and initial access without having to resort to complex matrix-based beamforming networks. Additionally, lens-based TX and RX beamforming is performed in the analog optical domain with zero power consumption and negligible latency bounded only by the time the light takes to travel through the lens. Photonic signal processing also reduces the number of RF components required at the remote radio unit (RRU) and the number of costly and power-hungry high-performance analog-to-digital/digital-to-analog converters (ADCs/DACs) required. The optical subsystems are ultra-wideband and frequency agnostic as only the front-end components (antennas, amplifiers) are RF frequency/band specific. Therefore, a single photonic system design may be operated at any band and, furthermore, existing installations may be modified/upgraded to operate in different bands with minimal component replacements needed. Finally, the presented architectures provide near unlimited beam-bandwidth product (BBP) with minimal power requirements and no external cooling. Theoretical analysis and experimental confirmation of the proposed architecture will both be reported, including a receiver with a nominal BBP of 36 GHz in a prototype system that consumed less than 300 W, thus yielding a power efficiency of beam formation of 8 W/GHz, which is more than a 6× improvement over the current state of the art.

INDEX TERMS Beamforming, microwave photonics, optical coherent detection, radio over fiber, wireless communications, beam bandwidth product.

The associate editor coordinating the review of this manuscript and approving it for publication was Derek Abbott.

I. INTRODUCTION

There is a growing trend in cellular communications to move toward higher carrier frequencies, which has led to the

incorporation of millimeter waves (mmW) in the latest 5G standard [1]. Future generations are exploring even higher frequencies, approaching the THz region for 6G and beyond [2]. However, the use of such higher frequencies results in a concomitant increase in free-space path loss (FSPL) which, consequently, requires an increase in antenna gain to compensate. Increased antenna gain reduces spatial coverage, which can be recovered by using larger beamforming arrays that allow for the simultaneous use of multiple dense high-gain beams to provide both wide spatial coverage and high array gain. Such an approach produces higher-gain beams that partially mitigate the increased FSPL but it also requires a higher level of BTS densification than we have today to compensate for higher path loss, wider bandwidths, and need for Line-of-Sight (LOS) links [3]. This higher level of densification increases backhauling needs, which is costly and not always available.

The capability of supporting a dense beamspace is an enabler for Massive Multiple-Input Multiple-Output (M-MIMO) [4], which has received considerable attention in the past decade and support for which has also been included in Releases 13-14 for LTE and Release 15 for New Radio/5G. M-MIMO systems use an excess of antennas at the BTS to achieve increased network capacity, improved coverage, and high spectral efficiency, all of which increase with the number of radiating elements. While M-MIMO is today becoming a reality in the mid-band spectrum, some believe that the expected BTS densification created by using higher carriers will cause a decrease in the number of active users per cell so that the advantages for M-MIMO at mmW and above may decrease. To this concern, we first point out that the dense beamspace attainable through massive MIMO is desirable not only to support a large number of users, but also to increase mobility performance even for a few users. Indeed, the increased spatial resolution supported by a dense beamspace allows better tracking mobile users. Furthermore, we would argue that this line of thinking may be dictated by the current challenges in implementing a *truly* massive MIMO all-electronic architecture. In fact, BTS architectures that support an arbitrarily large number of antennas with a very large BBP could decrease densification and associated backhauling needs, at least for those scenarios where good LOS can still be maintained, e.g., wireless broadband access in suburban or rural environment, wireless backhauling in point-to-multipoint configuration, stadiums, convention centers, airports, etc. Since the proposed architectures will be shown to also allow for a drastic reduction in RF components as well as DACs/ADCs, their benefits can find wider applicability and go beyond the scenarios listed earlier.

In the ultimate case of an infinite number of radiating elements, the aperture approaches a spatial continuum and the transmitted waveform, properly compensated for the propagation channel characteristics via precoding, is conceptually analogous to a holographic profile—see [5] where the concept of ''Holographic Massive MIMO'' was first introduced. Additionally, large arrays mitigate many impairments such as hardware imperfections, phase noise, nonlinearities, quantization errors, noise amplification, intercarrier interference, and also inter-symbol interference [6], [7], [8], [9]. To take advantage of the potential benefits offered by large arrays, architectures must support a large number of antenna elements and be capable of wideband beamforming with simultaneous multi-beam and multi-band operation, all of which are features in high demand among service providers.

The current trend requiring the BTS to support ever increasing bandwidths, number of antennas, and number of bands is already putting a strain on all-electronic implementations which, ultimately, will not be able to support a dense and wideband *holographic* beamspace. State-of-the-art all-electronic systems have difficulty covering a wide frequency range and maintaining phase synchronicity among numerous antenna elements, especially at high carrier frequencies. Fully digital beamforming solutions are expensive and suffer from high power consumption as the number of RF channels equals the number of antennas; also, they do not scale well when multiple bands need to be supported. Analog/hybrid beamforming helps reduce the cost of fully digital solutions but is handicapped by limited-resolution phase shifters, beam squint, and impaired spatial multiplexing capabilities. As the array size grows large and multi-band support is introduced, all-electronic implementations do not scale well. The cost and the power consumption of the RRU skyrocket while beamforming quality degrades due to the loss of synchronization between channels—even if a common signal reference is distributed amongst the radiating elements. Physical layout problems of routing electrical traces to multiple feeds and the sensitivity to the trace lengths at high frequencies arise when many antennas are used [10]. Furthermore, microwave I/Q up-converters, which are widely used to achieve single-sideband up-conversion in a variety of systems today, offer limited operating bandwidth and suffer from I/Q power and phase imbalance due to the frequency dependence of electronic mixers, power dividers, and hybrid couplers [11].

In contrast, the Fourier-based opto-electronic architectures presented here preserve spatial and temporal coherence, regardless of the number of antenna elements, thus enabling either analog or fully connected hybrid beamforming supporting a wideband and dense beamspace for both TX and RX. In the proposed implementation, the common optical module not only allows for a reduction in RF-component count, but also provides additional degrees of freedom thanks to wideband, parallel optical processing. The common optical part of the BTS remains the same regardless of the frequency band(s) used and naturally supports multi-band operation given the wide bandwidth available at optical frequencies. As such, if necessary, the antenna array can be changed to suit the utilized radio frequency bands,[1] assuming the role of the ''plug-in'' part of a modular, ''plug-and-play'' BTS design, while the optical part of the BTS architecture

[1] In the case of a wideband or multi-band design, there would be no need to change the antenna.

would be fixed because of its frequency independence, thus reducing drastically the bill of materials. By comparison, all-electronic BTSs have components that are finely tuned to the frequency bands of operation, making it difficult and/or costly to support multiple bands of operation and a large number of antenna elements. Such modularity is highly desirable, as it enables future scalability as new spectrum becomes available for 5G/6G, and facilitates vendor-neutral host deployments envisioned by the emerging Open RAN (O-RAN) initiative [12].

Recent advances in microwave, or RF, photonics have brought the vision of a modular architecture outlined above closer to reality in practical implementation and commercial viability. Thanks in part to the development of high-power, high-linearity photodiodes (PDs), there is a growing consensus that RF-photonic solutions for mmW/sub-mmW wireless applications can provide a substantial advantage over comparable all-electronic techniques [13], [14]. Furthermore, the maturity of photonic integrated circuits (PICs), which leverages the infrastructure from the semiconductor manufacturing industry, has led to ultra-small, broadband, monolithically integrated electro-optic (E/O) modulators, low-noise frequency synthesizers, chip-scale signal processors with enhanced spectral resolution, and the complete integration of light sources, modulators, and detectors in a single chip-scale photonic processor that offers multifunctional and reconfigurable operation similar to its electronic counterparts [15]. The benefits brought by RF photonics include wideband channelization, low-loss signal transport, freedom from electromagnetic interference, true-time delay wideband beamforming, lightweight and flexible cabling, and the availability of wideband adaptive optical signal processing [16], [17]. Furthermore, the cost and power-consumption challenges of fully digital beamforming that plague all-electronic implementations become less problematic in an electro-optic approach as it allows for a drastic reduction of RF component count.

Photonic up- and down-conversion for generating and processing high-quality RF waveforms exemplifies the broadband advantages of photonics where the only high-frequency hardware are amplifiers, work in tandem with the receiver's up-converting E/O modulators and the transmitter's photodiodes [18], respectively. Accordingly, the electronic processing hardware need only operate at lower frequencies determined by the information bandwidth (IBW) and/or IF(s) of the system. Furthermore, fiber-optic antenna feeds are characterized by extremely low loss, offering the system designer more degrees of freedom in architectural choices. This design flexibility allows, for example, low-cost RRUs where only the plug-in antenna arrays and related up/down-conversion equipment (E/O modulators and photodetectors) are deployed at a remote location.

A. ORGANIZATION OF WORK

This paper starts with an overview of the proposed BTS architecture and its enabling technologies in Section II. Section III describes lens-based transmitter beamforming. The receiver architecture is covered in Section IV, and architectural extensions supporting multi-band and multi-sector functionalities are given in Section V. Recent experimental results are reported in Section VI. A summary and concluding remarks are offered in Section VII. Appendices provide additional technical details and formalize the mathematics that underpin the approach.

II. THE PROPOSED NOVEL BTS ARCHITECTURE EXPLOITING OPTO-ELECTRONIC PROCESSING

A. ENABLING TECHNOLOGIES

The entire spectrum of present and future wireless radio communication is a minuscule fractional bandwidth of an optical carrier frequency. Indeed, 100 GHz of RF bandwidth constitutes merely 0.05% of a 200-THz carrier corresponding to an infrared wavelength of 1550 nm. Furthermore, the short optical wavelengths enable signal-processing methods that are not practical at radio-wavelength scales.

To take advantage of the opportunities presented by optical processing of electronic signals, conversion between the electrical and optical domains must be coherent both temporally and spatially, so as to preserve both amplitude and phase information present in the signals and across the array antenna. Thus, by employing a single laser source as the optical medium for up-converting RF signals, temporal coherence is automatically preserved during the conversion process, so long as the maximum pathlength difference between antenna elements does not exceed the coherence length. However, to preserve the phase-front of the up-converted RF wave, spatial coherence is also required. Maintaining such coherence, or synchronization, among multiple elements of a phased array, be it at the transmitter or the receiver, is recognized as a major challenge in all-electronic systems. This is especially true for high frequencies or short wavelengths, which may seem to be exacerbated by the conversion to vastly shorter, optical wavelengths.

To this end, the problem of maintaining spatial coherence across large receive arrays was solved by employing an active feedback loop to compensate in real time for mechanical, acoustic, and thermal perturbations that inevitably subject signals in optical fibers to micro-fluctuations that add phase noise—see [19], [20] for more details. This phase-feedback compensation preserves the RF phase front upon up-conversion from the RF to the optical domain, which enables the use of an optical lens to perform all of the beamspace processing, i.e., imaging, using conventional free-space or integrated optical elements. In this case, one literally forms an image of the RF beamspace, but in the optical domain. In so doing, all lens-based RF beamspace processing is performed with a latency limited only by the speed of light (i.e., nanoseconds), it consumes no power, and it does so with a virtually unlimited BBP, which is a measure of the number of simultaneous beams being processed at their maximum instantaneous bandwidth. Lastly, the entire beamspace

processor requires no external cooling and occupies a small physical volume.

The distribution of coherence across an array is further simplified by the development of a tunable optical paired source (TOPS) and tunable optical local oscillator (TOLO) that enable optical generation of high-purity, widely tunable RF carriers and their modulation with baseband (BB) signals [21], [22]. As a result, electronic signal processing takes place only at low baseband and intermediate frequencies using well-known techniques and low-cost, widely available components.

Finally, the development of broadband, high-efficiency electro-optic modulators [23], [24], [25], [26] and high-power, highly linear photodiodes [27] enables straightforward high-fidelity conversion between optical and electrical domains at the relevant frequencies and powers.

B. ARCHITECTURAL OVERVIEW AND ADVANTAGES

Utilizing the aforementioned technologies, we have demonstrated BTS architectures that offer both simplicity and improved flexibility compared to existing and presently contemplated all-electronic solutions. The architectures are highly modular, with the optical system being frequency agnostic and the electronic processing operating at only baseband or low intermediate frequencies (BB/IF).

In these novel RF-photonic BTS architectures optical up- and down-conversion are used to generate IF/RF and RF/IF signals, respectively, for simultaneous multi-user/multi-beam transmission and reception over a wide range of frequencies. The enabling technologies leading to this architecture have been demonstrated experimentally by the Authors in various publications, but we report here for the first time the whole TX/RX system, its mathematical modeling, and the latest experimental results. We will also compare the proposed architectures with all-electronic implementations and how they would fit in today's RAN architecture.

In the transmit implementation, the RF carrier is obtained as a beat frequency between two optical signals such that the modulation of either or both optical signals yield a respective modulation of the RF carrier. The pure RF carrier tone having 1-Hz line width and a continuous tuning range of 0.5–100 GHz is generated using a Tunable Optical Paired Source (TOPS), where two conventional semiconductor lasers are phase locked via modulation-sideband injection [21]. Synchronization across all the TX array elements is derived from using the same laser pair to drive all phased-array elements, which preserves temporal coherence between all antenna feeds. User data is applied to one of the two lasers using an E/O modulator. Digital precoding may be applied prior to optical up-conversion to realize fully connected hybrid beamforming but is not required for analog beamforming. We point out that even in the case of mere analog TX beamforming, the system can still generate multiple wideband beams simultaneously. The transmitter architecture allows for beamforming at any frequency within the tunability window of the lasers, which can span beyond 100 GHz. This approach is particularly well suited for RF carriers at mmW and above due to its capability of maintaining phase coherence for an arbitrarily large number of antennas, and offers advantages over other implementations that include low-loss transmission, minimum phase noise, light weight, ultra-wideband operation, high coherence, simultaneous multi-beam, and multi-band support.

The RF signal is obtained from the beat signal arising from the combination of the data modulation sideband with the second laser of the TOPS (functioning as an Optical Local Oscillator, OLO), using a high-power photodiode feeding each antenna element. Notably, beamforming is performed prior to combining the two lasers, using an optical lens as the equivalent of an analog combiner. This analog beamforming configuration enables the transmission of multiple beams simultaneously without a digital precoder and using a single DAC per beam, as opposed to having to use one DAC per antenna (digital beamforming) or one DAC per antenna sub-array (hybrid beamforming). This allows for a significant reduction in the number of DACs required compared to an all-electronic multi-beam implementation. (See [28] for a review of DARPA's interest in wideband, multi-band, and multi-beam mmW wireless systems and related challenges in all-electronic implementations.) The data-modulated laser is launched into free space from a fiber termination located in the input (front focal) plane of the lens, which spreads its energy uniformly over the output (back focal) plane. The output plane is populated with an array of "pickup" fibers that capture the optical energy and convey it to the photodiodes that feed the array elements. The OLO is also launched into free space from the input plane of the lens, and likewise captured by the pickup fibers. The transmitted beam direction is determined by the location in the input plane of the optical fiber carrying the modulated data, thanks to the property of the Fourier transform that a translation in one domain becomes a phase in the other. These phase shifts are preserved in the beat signal. In this way, the required steering phases are automatically applied to each array element. The desired output beam is selected using an array of fibers in the front focal plane and an optical switch/router.

The receive architecture also uses an optical lens for beamforming and affords the ability to apply arbitrary complex weights to each array element prior to beamforming using only broadband, low loss, dispersionless optical components. This weighting capability is enabled through the use of optical modulators that up-convert input signals to sidebands on an optical carrier. Modulator output fibers are arranged in a bundle in the input plane of the beamforming lens. The lens performs a spatial FT thus converting the element phases that arise from the incident RF signals' angle of arrival into a position in the output plane, i.e., an imaged spot. Lens-based RX beamforming allows parallel processing of multiple simultaneous beams at negligible latency prior to digitization, thus allowing a reduction of ADCs and the use of commercial-off-the-shelf (COTS) ADCs operating at the

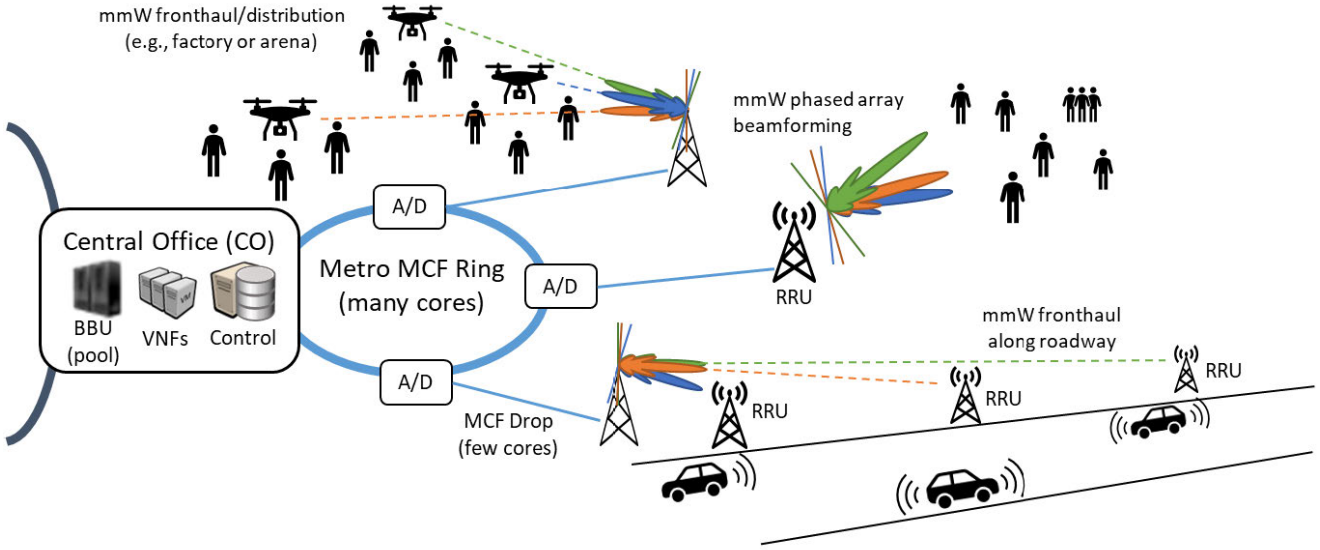

(Figure adapted from Johanssen, *et al.*, "ARoF-Fed Antenna Architectures for 5G Networks," IEEE OFC 2019.)

FIGURE 1. Architecture for analog radio-over-fiber (RoF) fed antennas in wireless networks, as proposed in Ref. [29]. (BBU: Baseband Unit; VNFs: Virtual Network Functions; A/D: Analog-to-Digital conversion; MCF: Multi-Core Fiber; RRU: Remote Radio Unit).

information rate or IF with high effective number of bits (ENOB). After beamforming, the optical beams are down-converted to a chosen, tunable IF using a TOPS-derived OLO. Spatial coherence between the array elements is maintained using a closed-loop feedback scheme that monitors and compensates for fiber-induced phase variations in real time.

The advantages of the architecture described above can be summarized as follows:

- A universal opto-electronic architecture with near zero-latency analog/hybrid (fully connected) beamforming that: forms/processes all beams simultaneously, is independent of the specific bands supported and at the same time supports multi-band, multi-sector, and multi-beam capabilities with a high level of coherence across large antenna arrays. The common optical system can support multiple simultaneous bands via a widely tunable laser, thereby remaining frequency agnostic. We further point out that:
  - The BTS becomes more modular and future proof thereby facilitating incremental deployment and frequency re-planning.
  - Laser tunability and the absence of RF components fulfill the true promise of Software Defined Radios (SDRs) by replacing RF-based sampling with BB/IF sampling and processing.
- Simple and low-cost "plug-and-play" RRUs with no baseband processing requirements and minimal RF component count, i.e., no mixers, fewer filters, no LO routing network, and ADCs/DACs only in the baseband unit (BBU). The antenna array and RF amplifiers can be changed to suit the utilized frequency bands whereas the optical part of the BTS architecture would be fixed because of its frequency independence, thereby reducing drastically the bill of materials.
- Large BBP ensured by spatial processing via an optical lens beamformer, whose operation is independent of the number of antennas or beams.
- High-frequency hardware requirements involve only the receive up-converting E/O modulators and the PDs at the transmitter, whereas the electronic processing hardware operates at the much lower BB/IF frequencies.
- Use of an optical lens alleviates the implementation problems related to realizing fully connected transmit beamformers that surpass all-electronic solutions. Additional benefits include:
  - Utilization of DACs/ADCs operating only at BB/IF frequencies.
  - Analog parallel formation/processing of multiple simultaneous wideband beams at the speed of light with negligible latency. On the receiver side, beamforming is performed prior to digitization, greatly reducing the number and required performance of the needed ADCs.
  - The ability to transmit multiple beams simultaneously even when only analog beamforming is used, i.e., without a digital precoder – see Section III.
  - Simplified tracking at mmW bands via real-time imaging of the electromagnetic environment and cellular sources.

The advantages listed above favor applications that require handling large BBPs at mmW and also sub-mmW frequencies when, for example, M-MIMO is employed. This includes scenarios where multiple wideband transmit/receive beams must be processed simultaneously as in broadband access, point-to-point backhauling, fronthauling, powering in/out-door hotspots, tracking multiple drones or vehicles requiring broadband links, etc. For illustration of example applications, see Fig. 1 [29].

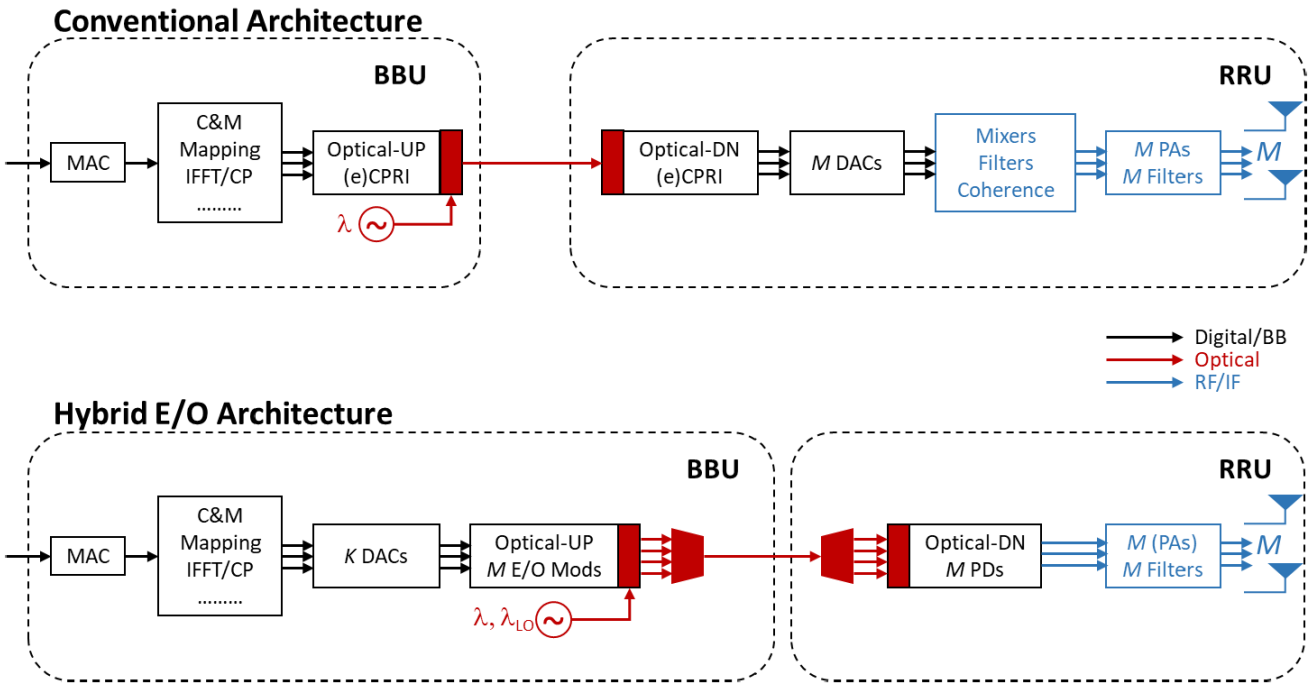

FIGURE 2. Schematic of a conventional (top) and E/O-hybrid (bottom) BTS transmitter, including BBU and RRU, with *M*-element antenna arrays, serving up to *K* users simultaneously. (MAC: Medium Access Control; C&M: Control and Management; IFFT/CP: Inverse Fast Fourier Transform/Cyclic Prefix; UP/DN: Up-/down-conversion; (e)CPRI: (enhanced) Common Public Radio Interface; DAC: Digital-to-Analog Converter; PA: Power Amplifier; E/O Mod: Electro-optic Modulator; PD: Photo(diode) Detector).

In the next Sections, the details of the transmit and receive architecture will be discussed.

III. THE TRANSMITTER ARCHITECTURE

The proposed opto-electronic transmitter and its conventional counterpart, including the BBU and the RF Processing Unit or RRU, are shown in Fig. 2. The signal paths of digital/baseband, optical, and IF/RF signals are color-coded as black, red, and blue, respectively. In the conventional architecture (top of Fig. 2), we show a digital optical link used to connect the BBU to the RRU. The latest version of this digital interface is called Enhanced Common Public Radio Interface (eCPRI) and its specifications were developed by Ericsson AB, Huawei Technologies Co. Ltd, NEC Corporation, and Nokia [30]. eCPRI is a digital radio-over-Fiber (D-RoF) link used for fronthauling in 5G, and it partly overcomes the capacity bottleneck of the previous CPRI used in LTE by moving some higher layer functions back to the RRU, somewhat reducing the benefits of centralization as well as making the RRU more costly and power hungry. The eCPRI specifications define many possible BBU/RRU splits; the one shown in Fig. 2 is known as interface II_D and allows for the least baseband processing at the RRU.

In contrast to the conventional architecture, the optical link between BBU and RRU in the opto-electronic architecture proposed here is an analog-RoF link. A-RoF not only solves the fronthauling capacity problem, but it also improves the degree of centralization of the architecture by moving DACs and ADCs out of the RRF (see bottom of Fig. 2). The analog link also allows a direct integration of the photodiodes used for down-conversion from optical to RF domain within the antenna itself. Alternatively, a bank of photodiodes may be laid out on a separate printed-circuit board (PCB) that communicates with the antenna-array PCB via high-speed RF connectors. Such arrangements allow very simple, low cost "plug & play" RRUs that require only DC power to bias the photodetectors in addition to the optical fiber(s) that carry signals [31]. Since each antenna of the array is fed a distinct signal, the number of optical feeds equals the number of antennas. Accordingly, the optical signals may be delivered to the RRU using a fiber bundle, with each fiber dedicated to a specific antenna, or in a single fiber by employing wavelength-division multiplexing or other signal encoding schemes [32], [33].

Note that whereas the conventional RRU requires both baseband and IF/RF processing, no baseband processing takes place in the opto-electronic RRU, which, in addition, uses fewer RF components and employs no dedicated circuity to maintain coherence between feeds. Thus, any change in frequency band that needs to be supported requires replacing only the simple RRU or just its antenna, and no other change either at the RRU or the BBU, except for re-tuning the lasers, which can be done via the Service Provider's Operation Support System.

For comparison, consider an all-electronic transmitter RRU of Fig. 3 that supports multiple (*B*) bands and is shown

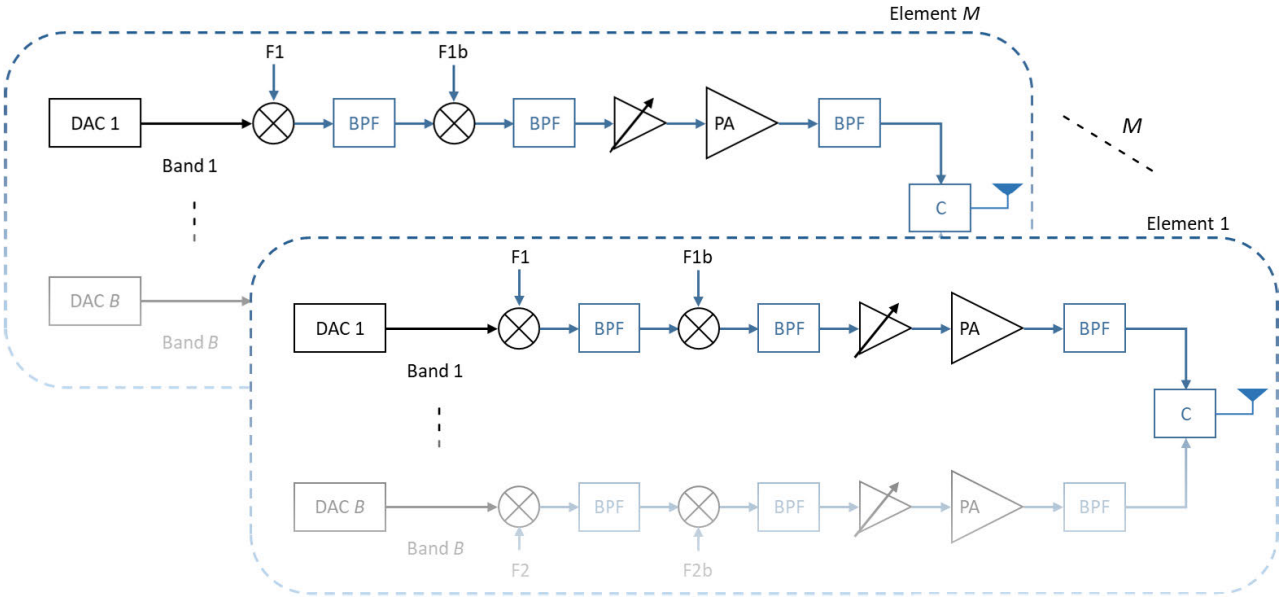

FIGURE 3. All-electrical transmitter with multi-band option. (DAC: Digital-to-Analog Converter; BPF: Band-pass Filter; C: Combiner).

in a dual-heterodyne architecture with multiple mixers and bandpass filters. The I/Q signals for Band 1 are converted to a modulated waveform before the DAC to take advantage of digital modulation that can be performed with minimal gain or phase errors. The low IF is up-converted to an RF signal in the range of 26 GHz before getting up-converted again to the final mmW frequency. Up-conversion is performed in multiple stages, depending on the final transmit frequency, to mitigate conduction loss and phase synchronization errors when distributing millimeter-wave-frequency LOs to the array elements. The band-pass filters after the mixers attenuate unwanted spurious mixing signals and the final power amplifier (PA) brings the main signal up to the desired level. The final band-pass filter cleans up the spectrum after the PA and before the B bands are combined and radiated by the antenna.

TABLE 1. Number of components used in the BTS transmitter implementation, for both a conventional "all-electronic" architecture and the proposed opto-electronic (O/E) one. The transmitter supports B bands sent to K users via a single wideband antenna array with M antenna elements ($K < M$).

	All-Electronic [n-stage up-conversion]	O/E
DACs	MB	K
Combiners/Duplexers	M	-
RF Mixers	nMB	-
RF Power Amplifiers	MB	-
Filters	$(n+1)MB$	K
Optical Modulators	-	K
Photodetectors	-	M
EDFAs (optional)	-	K
TOPS	-	B

As shown in Table 1, the proposed opto-electronic architecture allows for a drastic reduction in RF component count by introducing a common optical module that supports any number B of bands with either a single wideband antenna array or multiple switchable/swappable band-specific antenna arrays. Frequency-dependent RF mixers, filters, and power amplifiers are replaced by optical modulators and photodetectors. Whereas the number of band-dependent RF components is proportional to the product MB, the number of optical components grows either with the number M of antennas (PDs, filters) or the number K of simultaneous users (modulators, erbium-doped fiber amplifiers (EDFAs)).

The opto-electronic implementation discussed here allows for a good demarcation between BBU and RRU, with a simple, low-cost RRU where antenna arrays can be simply swapped in and out while the core optical portion remains the same regardless of the utilized frequency bands. Novel optoelectronic lens-less implementations of MIMO transmitters have been previously reported by the Authors in [34] and [35]. The experimental results reported in [34] confirmed the capability of conveying independent data over two different spatial beams simultaneously, using the same RF carrier. Although optoelectronic lens-less implementations of MIMO transmitters are interesting, this paper focuses on architectures supporting lens-based beamforming at the transmitter as they allow performing analog or fully connected hybrid beamforming [36], [37], [38] with the many benefits mentioned in the previous sections.

The capability of implementing a fully connected hybrid beamformer opens the door to enabling "virtual sectorization" where users can be grouped by virtual sectors using a bank of precoders [39]. Virtual sectorization enables separated baseband processing and minimization of signaling overhead by allowing downlink training to be performed in parallel, and each UE would only need to feed back the intra-group channels, leading to a reduction of both training and

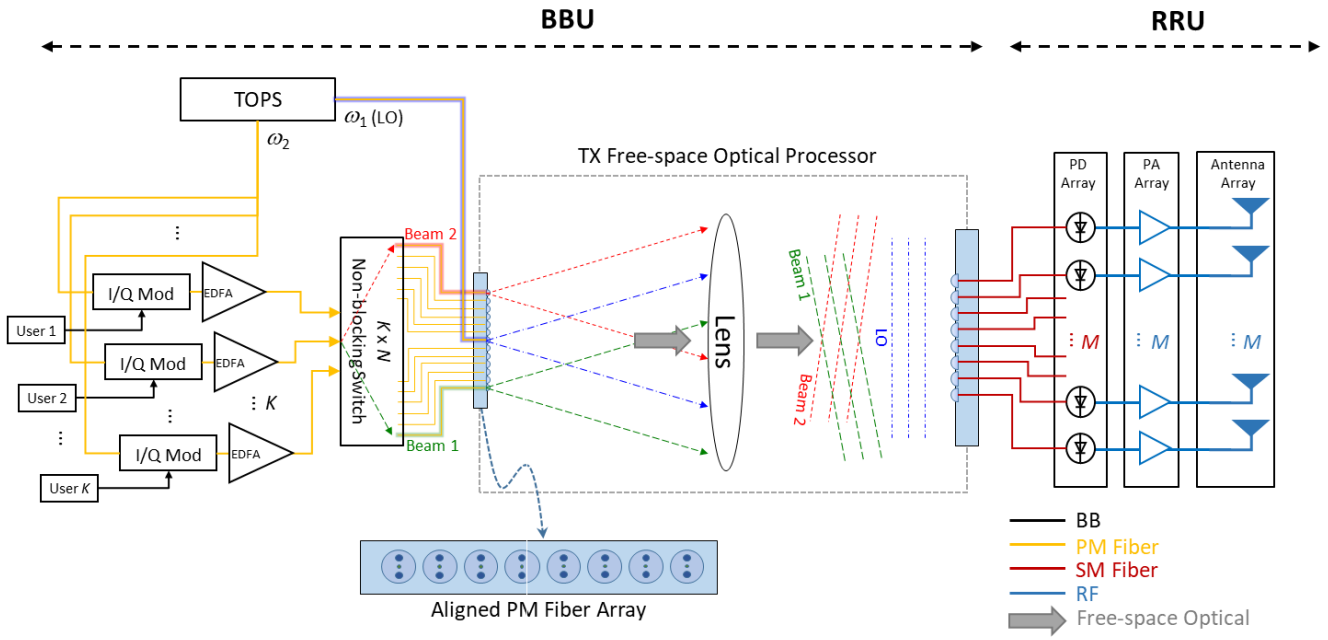

FIGURE 4. Transmitter with lens and conventional I/Q modulators.

feedback overhead by a factor equal to the number of virtual sectors. When downlink training and CSI feedback from the user terminals to the BTS are greatly reduced, then using a large number of antennas at the BTS becomes potentially suitable also for frequency-division duplex (FDD) systems whose overhead for CSI estimation scales with the number of BTS antennas [40].

An additional important aspect of the proposed architecture is that multiple simultaneous beams can be generated even in a purely analog beamforming implementation. This provides better scalability through a substantial reduction of complexity in the baseband processing performed at the transmitter, because the digital precoder for hybrid beamforming is not needed and thus there is no need to process many wideband sources.

The same goal can also be achieved in RF by using all-electronic lenses, an approach called Beam Space MIMO in the wireless community [41], but these kinds of lenses present several practical limitations. All-electronic lens-like beamformers, such as Rotman lenses and Butler matrix designs, are well known [42], but do not scale well to mmW frequencies and accompanying wide operational bandwidths due to losses and dispersion that increase with frequency. Furthermore, matrix-based beamforming networks are power consuming and become increasingly complex as the number of antennas grows. While dielectric lenses that function directly at the RF transmit frequency have been studied for mmW beamforming [43], they are exceedingly bulky due to the inherent volumetric scaling of focal-plane array designs with the aperture size, and hence with the number of array elements. In addition, they suffer from crosstalk between closely spaced metallic radiating elements. As an example, AT&T reported in 2015 the use of a Luneburg lens to create spatial sectors within a stadium environment [44]. It was shown to provide a substantial increase in data rates both in aggregate and within each spatial sector, but the lens was bulky and weighed several hundred pounds. Transmissive metamaterial-based surfaces and lenses, such as so-called Huygens meta-surfaces, have been recently proposed to reduce beamforming complexity [45], [46], [47], [48], [49], offering a compact beamformer amenable to planar fabrication. However, such structures are inherently band-specific, functioning only within a single design frequency band. In contrast, in the transmit architecture presented here, beamforming is performed in the optical domain, combining the complexity-reduction advantages of lens-based beamforming with an extremely wideband, frequency-agnostic, scalable, compact implementation, where the radiating elements are optical fiber terminations with negligible crosstalk.

Figure 4 shows a schematic diagram of the transmitter's architecture. A TOPS is the optical source used for powering the transmit antenna array, with the frequency offset between the two coherent beams equal to the carrier frequency of the transmitter RF wave. Conventional I/Q modulators impart the desired signals on the transmitted waves. According to Fig. 4, one of the TOPS beams is split K ways corresponding to K users among N spatial sectors covered by the BBU, and each of the resulting K beams is modulated individually by the signal destined for the corresponding spatial sector. An optical switch/router routes the I/Q modulated optical signals as needed for the spatial-sector mapping.

The lens converts the beams emanating from the optical-fiber array to approximately plane waves that are captured by the pick-up fiber array. In addition, one of the input fibers is dedicated to carry the OLO beam so that each of the pick-up fibers receives both the OLO and the data-modulated beams. The pick-up fibers carry the optical signals to antenna-coupled photodiodes that convert them to RF. The optical phase profile introduced by the lens across the pick-up fiber array becomes an RF phase profile across the antenna array that forms corresponding radiated electromagnetic beams. In the sub-sections below, we provide more detail on the various blocks shown in Fig. 4.

A. TUNABLE OPTICAL PAIRED-LASER SOURCE

Optical generation of radio waves relies on photo-mixing of two optical beams having frequencies separated by the desired RF frequency—see Appendix B. For example, consider two optical signals with electric field amplitudes U_1, U_2 described by:

$$\begin{aligned} U_1(t) &= \sqrt{I_1}\cos\left(\omega_1 t + \varphi_1(t)\right) \\ U_2(t) &= \sqrt{I_2}\cos\left(\omega_2 t + \varphi_2(t)\right), \end{aligned} \tag{1}$$

where I_1 (I_2) is the intensity of the first (second) optical beam, ω_1 (ω_2) is its angular frequency, and φ_1 (φ_2) is its phase offset. When combined on a photodiode, the two optical signals in (1) yield an electrical signal proportional to the time-averaged optical power:

$$P = \frac{1}{2}\left\langle |U_1(t) + U_2(t)|^2 \right\rangle, \tag{2}$$

where, for RF generation, the averaging (denoted by angled brackets) takes places over time scales long compared to the optical oscillation frequencies but short compared to their difference $|\omega_1 - \omega_2|$. With definitions (1), the detected power (2) becomes:

$$P = \frac{I_1}{2} + \frac{I_2}{2} + \sqrt{I_1 I_2}\cos\left[\left(\omega_1 - \omega_2\right)t + \varphi_1 - \varphi_2\right], \tag{3}$$

where the high-frequency terms vanish due to the bandwidth-limited response of the photodiode. The first two terms in (3) are constant for unmodulated optical beams whereas the third term is oscillatory at a frequency equal to the difference $|\omega_1 - \omega_2|$. The phase offset of the generated electrical signal equals the difference of the optical phase offsets $(\varphi_1 - \varphi_2)$.

In real-world devices, the optical phase offset φ fluctuates randomly in time. These phase fluctuations contribute to the finite spectral linewidth of a laser, which in a typical inexpensive semiconductor laser is in the range of a few MHz and sets the relevant time scale for φ variation at tens of nanoseconds. As a result of the random phase fluctuations, combining the outputs of frequency-offset independently operating lasers on a photodiode yields an RF signal with frequency variation, and a spectral-line profile equal to the convolution of the individual spectral-line profiles of each laser. With typical laser line widths of tens of MHz, the resulting RF linewidths would be unsuitable for most applications in wireless communications. The spectral linewidth problem may be resolved in one of two ways:

1) making the linewidth of the individual lasers narrower by employing expensive lasers; or
2) ensuring that $\varphi_1 = \varphi_2$ so that laser phase fluctuations do not contribute to the RF spectral linewidth.

The TOPS follows the second approach as a low-cost alternative to employing high-stability laser sources. To this end, the output of the first (source) laser is modulated and one of the modulation sidebands is used to injection lock the second (clone) laser. Wide TOPS tunability is obtained by the combination of tuning the modulation frequency and harmonic-comb generation in a saturated electronic amplifier feeding the E/O modulator used to modulate the source-laser output. The TOPS, its operation, and performance have been described in detail in [21] and [22]. The experimental results reported in [21] confirm the generation of continuously tunable signals from 0.5 to 110 GHz while preserving the timing jitter of the reference. With this solution, two inexpensive semiconductor lasers are made mutually coherent so that, when their outputs are mixed on a photodiode, optical contributions to the phase noise cancel out and a low-phase-noise RF signal is generated at the RRU.

For multi-band support, a single TOPS can be used if the bands can be supported by the same wideband antenna and the spectral separation is less than the supported bandwidth of the photodiodes (which can be as wide as 100 GHz or more). Alternatively, multiple TOPS can be used, each generating a pair of phase-locked optical beams spectrally separated by the desired RF carrier for each band, where the separation between the frequencies in different TOPS pairs is well above the photodiode bandwidth, to avoid generating unwanted signals through mixing of inter-TOPS pairs.

B. DATA MODULATION

According to Fig. 4, one of the TOPS beams is split K ways corresponding to K users among N spatial sectors covered by the BBU. Each of the resulting K beams is amplified and modulated individually by the signal destined for the corresponding spatial sector using a single I/Q modulator. Preferably, these modulators are biased and fed to produce single-sideband, suppressed carrier (S3C) output, to minimize generation of spurious out-of-band signals upon mixing with the OLO.

C. FREE-SPACE OPTICAL PROCESSOR

a: SWITCH AND INPUT FIBER ARRAY

The outputs of the data modulators are directed to the fiber array at the input plane of the FT lens through a non-blocking optical switch, providing the ability to direct any of K user data streams into any of the N input fiber positions, where each input position corresponds to a separate transmit beam direction.

To ensure complete coverage of the antenna array's beamspace, i.e., a dense array of M beams for an

M-element antenna array, the number of input fibers should be $N = M$. Moreover, the input fiber array and output fiber arrays should be spaced according to the relation (in the small angle/paraxial limit):

$$Nd_i d_o = \lambda F, \tag{4}$$

where d_i (d_o) is the input (output) fiber spacing, λ is the optical wavelength, and F is the focal length of the FT lens. This relation ensures that the correct steering phases are obtained, namely that the phase at output fiber m for a signal directed to input fiber n will be:

$$\phi_m = 2\pi \frac{mn}{N}. \tag{5}$$

See Appendix C for additional details (presented in the context of receive beamforming, but the Fourier phases in relation to the fiber positions are the same).

b: FOURIER TRANSFORM LENS AS A BEAMFORMER

The lens-based beamforming process may be understood formally by noting that in the paraxial approximation, a lens converts the optical field distribution in its front focal plane to its spatial Fourier Transform (FT) in its back focal plane [50]. That is, given the complex electric field distribution one focal length F to the left of the lens:

$$U_{-F}(\mathbf{x}) = U(x, y, z = -F), \tag{6}$$

the field distribution at a distance F to the right of the lens becomes:

$$\begin{aligned} U_F(\mathbf{u}) &= U(u, v, z = F) \\ &= \frac{1}{F\lambda} \int U_{-F}(\mathbf{x}) \exp\left(-j2\pi \frac{\mathbf{u}\cdot\mathbf{x}}{F\lambda}\right) \mathrm{d}x\,\mathrm{d}y \end{aligned} \tag{7}$$

where coordinates $\mathbf{u} = (u, v)$ are used for the output focal plane to distinguish them from the input-plane coordinates $\mathbf{x} = (x, y)$. λ is the wavelength of light used in processing. For a point source at the location $\mathbf{x}_m$ of the m^{th} fiber in the input focal plane, the input field distribution is:

$$U_{-F}(\mathbf{x}) = F\lambda U_m \delta(\mathbf{x} - \mathbf{x}_m), \tag{8}$$

and the field distribution (7) in the output focal plane is:

$$U_F(\mathbf{u}) = U_m \exp\left(-j2\pi \frac{\mathbf{u}\cdot\mathbf{x}_m}{F\lambda}\right). \tag{9}$$

This corresponds to a plane wave with a wave-vector $\mathbf{k}_m$ given by:

$$\mathbf{k}_m = -\frac{2\pi}{\lambda}\left(\frac{\mathbf{x}_m}{F}\right) \tag{10}$$

incident on the pick-up fiber array. Under narrowband approximation, harmonic time dependence $\exp(j\omega_2 t)$ is understood in (9), where ω_2 is the frequency of the clone-laser output, so that:

$$U_F(\mathbf{u}, t) = U_m \exp\left(-j2\pi \frac{\mathbf{u}\cdot\mathbf{x}_m}{F\lambda}\right) \exp(j\omega_2 t). \tag{11}$$

Placing the fiber carrying the OLO beam, with frequency ω_1, at the center of the input array at $\mathbf{x}_0 = \mathbf{0}$ yields a plane wave with a null projection of the wave-vector onto the u-v plane:

$$U_F^0(\mathbf{u}, t) = U_0 \exp(j\omega_1 t). \tag{12}$$

Fields (11) and (12) combine at the output focal plane (u, v) where the optical signals are collected by lenslets placed at discrete locations $\mathbf{u}_n$, launched into single-mode fibers, and transmitted to the respective antenna-coupled photodiodes. The combined field $U_m^{\text{tot}}(\mathbf{u}_n, t)$, launched by the m^{th} fiber and picked-up by the lenslet in position $\mathbf{u}_n$, at the n^{th} photodiode is then:

$$\begin{aligned} U_m^{\text{tot}}(\mathbf{u}_n, t) &= U_F(\mathbf{u}_n, t) + U_F^0(\mathbf{u}_n, t) \\ &= U_m \exp\left(-j2\pi \frac{\mathbf{u}_n\cdot\mathbf{x}_n}{F\lambda} + j\omega_2 t\right) \\ &\quad + U_0 \exp(j\omega_1 t). \end{aligned} \tag{13}$$

D. PHOTODIODE/ANTENNA ARRAY

Signals (13) oscillating at the reference ω_1 and clone ω_2 frequencies propagate along the optical fibers from the pickup fiber array to the photodiodes. Co-propagation of the two optical signals along the same fiber enables superior beamforming performance because any fiber-induced optical phase variation cancels out when down-converting to RF. The photo-mixing of the signals (13) incident at photodiodes produces photocurrents proportional to the squared complex field amplitude (i.e., the instantaneous optical power) time averaged over many optical periods:

$$\begin{aligned} \left\langle \left| U_m^{\text{tot}}(\mathbf{u}_n, t) \right|^2 \right\rangle &= \left\langle \left| U_F(\mathbf{u}_n, t) + U_F^0(\mathbf{u}_n, t) \right|^2 \right\rangle \\ &= |U_m|^2 + |U_0|^2 \\ &\quad + 2\,|U_m U_0| \cos\left(\omega_{\text{RF}} t - \vartheta_{n,m} + \phi_m\right), \end{aligned} \tag{14}$$

where $\omega_{\text{RF}} = \omega_2 - \omega_1$, $\vartheta_{n,m} = 2\pi \mathbf{u}_n \cdot \mathbf{x}_m / (F\lambda)$, and ϕ_m is independent of the position $\mathbf{u}_n$ and is defined as $\phi_m = \arg(U_m U_0^*)$.

The first two terms in (14) represent a DC offset whereas the last term is oscillatory at the RF frequency ω_{RF}. The $\mathbf{u}$-dependent phase $\vartheta_{n,m}$ provides for RF beamforming as long as the positions $\mathbf{u}_n$ of the pickup fibers in the u-v plane are a scaled replica of the antenna positions $\mathbf{U}_n$ in the antenna-array plane (U, V). In this case, the position of the m^{th} input fiber $\mathbf{x}_m$ determines the direction of the transmitted RF-beam propagation defined by the RF wave vector $\mathbf{K}$ so that the RF phase at the n^{th} antenna element is equal to:

$$\mathbf{U}_n \cdot \mathbf{K} = -\frac{2\pi}{F\lambda} \mathbf{u}_n \cdot \mathbf{x}_m. \tag{15}$$

Notably, according to (14), any modulation of the optical amplitude U_m or phase ϕ_m carries over to the amplitude and phase modulation of the transmitted RF beam. Naturally, the signals that modulate the amplitude and phase are the precoded data, taking the Channel State Information (CSI)

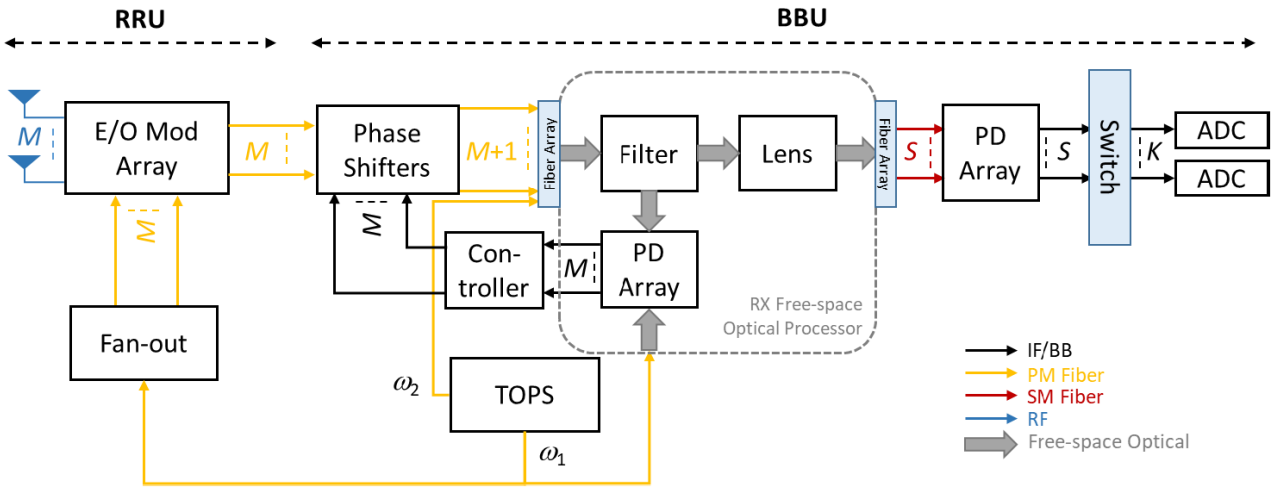

FIGURE 5. Schematic of the whole receiver and its constituent blocks.

into consideration, so that the receiver obtains a distortion-free information-carrying signal.

At this stage, high-power, high-linearity, charge- compensated modified uni-travelling carrier (CC-MUTC) photodiodes [27] can be integrated directly, or with the use of power amplifiers, into tightly-coupled-array antennas known for their wideband operation, large scan angles, and low-profile design. The experimental results reported in [51] confirm that high-power, high-linearity CC-MUTC photodiodes, which enable high-frequency, high-gain, low-noise-figure, and high-linearity photonic links, can be integrated into connected-array and tightly-coupled-array antennas. Optical excitation of a photodiode provides a balanced current source at the antenna feed, so that baluns or other complicated feed networks are not necessary, thereby significantly reducing cost and complexity.

To maintain the phase relations in (15) across the array, it is important to ensure identical time delays between the pickup fiber array and the elements of the antenna array. To avoid inter-symbol interference, the accuracy to which the fibers must have same length depends on the information bandwidth of the transmitted signal and is more stringent for signals with wider bandwidth. Typical bandwidths in 5G are around ∼1 GHz so that it is sufficient to ensure that the path length differential is kept under ∼7.5 cm. Even if this threshold is satisfied, however, note that the quality of the transmitted beam (e.g., array gain and sidelobe level) will degrade unless the paths are well matched to within a fraction of the RF carrier frequency. Calculations of beam patterns for a critically sampled 8-element array transmitting at 25 GHz indicate that to maintain sidelobes below –10 dBc, paths should be matched to within ∼λ/8, or 1 mm in glass fiber ($n = 1.5$). Additionally, in the case of multi-band support, if a total frequency range of 100 GHz is to be down-converted then it is necessary to ensure that path differentials are less than 0.25 mm. This is well within current capabilities, which allow an accuracy around 10 μm [52].

IV. THE RECEIVER ARCHITECTURE

A schematic block diagram of the receiver, including both BBU and RRU, is shown in Fig. 5, where RF waves are caught by the receiving antenna array. Behind each antenna is a low-noise amplifier (LNA) that boosts the captured signal before using it to modulate an optical beam at frequency ω_1 generated by TOPS, as shown in Fig. 5. Electro-optic modulators up-convert signals captured by the antennas to the optical domain, and optical fibers route the resulting modulated optical beams to a fiber array.

A. BEAM FORMATION

Optical beams emanate from the respective optical fibers and propagate in free space toward a FT optical lens, located one focal length, F, away. The lens collimates the diverging waves to plane waves where each of the M plane waves has a (different) direction of propagation that depends on the position of the corresponding fiber in the input array. The optical carrier and one of the sidebands are filtered out, and the remaining sidebands form an image on a photodetector array, or a pickup fiber array, located in the output focal plane, where it is combined with a TOPS-generated optical reference oscillating at frequency ω_2.

A distribution of distant sources produces electromagnetic field distribution at the antenna-array plane that is a Fourier transform of the source distribution. The up-conversion of the intercepted RF signals to optical domain preserves the phase relations between signals in different fibers. Therefore, the distribution of the optical field at the fiber array is directly proportional to the RF-field distribution at the antenna array, assuming a homothetic relation between the coordinates of the antennas and the coordinates of the fibers in their respective arrays.

Similar to the transmitter case discussed in Section III-C, the lens in the receiver of Fig. 5 performs a spatial Fourier transformation of the field distribution in one focal plane and outputs the result in the other focal plane. As a result, the optical field distribution at the output focal plane is the composition of two Fourier transformations operating on the spatial distribution of the distant sources. The composition of two Fourier transforms returns the original function subject to point reflection with respect to the origin. Since point reflection is a simple transformation that may be easily accounted for, the distribution of light on the photodetector or pickup fiber array corresponds directly to the spatial distribution of RF sources.

The simple analysis presented above shows that one may anticipate the optical image produced at the pickup fiber array in Fig. 5 to correspond to the distribution of RF sources. A more detailed derivation that explicitly assumes a finite number of channels in the system is presented in Appendix C. That analysis provides further insight into the image scaling and the emergence of artifacts such as grating lobes.

The first experimental demonstration of the beamforming capabilities of the receiver was reported in 2017 [53]. In that experiment, the 1×8 receiver was able to demodulate simultaneously two independent signals (4-QAM and 16-QAM) that shared a common carrier (15.94 GHz) and were transmitted by different locations so that the signals were imaged into two distinct spatial sectors. More recent results using a 1×15 receiver and reporting a new BBP record can be found in Section VI.

B. PHASE COMPENSATION

We note that in this architecture, M separate optical fibers convey the optical signals between the fiber fan-out and the free-space optical processor. As a result, maintaining spatial coherence, which is necessary for lens-based beamforming, requires active phase control to cancel environmentally induced optical phase variations [19], [20].

To this end, fibers arriving in the BBU pass through low-speed phase modulators that apply a bias voltage at each channel to compensate in real time for the random phase variations induced by acoustic, mechanical, and thermal perturbations. This active-feedback process ensures that the optical signals across the array remain spatially coherent, which allows for the use of Fourier optics to perform the spatial processing on all of the received RF signals. In practice, the same modulators used for the up-conversion of RF signals can also be used for the phase compensation, provided low-speed biasing electrodes are present. This approach simplifies the hardware and has the added benefit of avoiding any additional losses associated with coupling in and out of separate low-speed modulators. However, the downside of this approach is that modulator bias signals would have to be sent from the BBU to the RRU, adding to the volume of cables required to link them together. The best option in any deployed system would depend on the physical RRU-BBU separation: for short distances, the benefit of eliminating the separate low-speed modulators would likely outweigh the costs associated with providing feedback signals to the RRU; for long separation distances, it would likely be advantageous to have only lightweight, low-loss optical fibers between the BBU and RRU.

To obtain the feedback signal for compensation, an image of the fiber array is generated using the optical carriers that are reflected by the optical sideband filter. These carrier images contain the same phase perturbations as the sidebands, having traveled through the same segments of fiber with them. The carrier images are overlaid on a low-speed photodetector array with a large, collimated beam derived from the same laser of the TOPS that feeds the up-conversion modulators. Thus, the collimated laser signal mixes with the focused spots from the reflected carrier in each fiber so that each photodetector captures the beat between the signal in one channel and the common reference, Fig. 5. The outputs of these photodetectors are used to measure and compensate for mechanical/acoustic (< 20 kHz) phase variations within the fiber feed network in real time at a 200-kHz refresh rate via the aforementioned low-speed phase modulators.

C. DOWN-CONVERSION

The down-conversion of the intercepted signals to baseband or IF proceeds in a manner similar to that discussed in the context of the transmitter array, see Section III-D, with the difference in the analysis being that the wavelengths involved are selected to generate an IF signal rather than an RF one.

As discussed above and in Appendix C, after beamforming by the FT lens, the up-converted, beamformed optical intensity from all the antenna elements is incident on a photodetector array, or a pickup fiber array that subsequently feeds an array of detectors. The desired IF output from a given detector is obtained upon combination of the portion of the up-converted light distribution that impinges on that detector with the TOPS-derived OLO. Hence, the TOPS is configured to produce a frequency given by

$$\omega_{\mathrm{LO}} = \omega_1 + (\omega_{\mathrm{RF}} \pm \omega_{\mathrm{IF}}). \tag{16}$$

In the same manner used to obtain (3) and (B.4), we obtain the following expression for the total intensity at the n^{th} photodetector, located at position $\mathbf{x}_n$ in the image plane:

$$\begin{aligned} I_n(t) &= \left\langle |U_s(\mathbf{x}_n, t) + U_{\mathrm{LO}}(t)|^2 \right\rangle \\ &= I_s(\mathbf{x}_n, t) + I_{\mathrm{LO}}(\mathbf{x}_n) + 2\left\langle \Re\left[U_s(\mathbf{x}_n, t) U^*_{\mathrm{LO}}(\mathbf{x}_n, t)\right]\right\rangle \\ &= I_s(\mathbf{x}_n, t) + I_{\mathrm{LO}}(\mathbf{x}_n) \\ &\quad + 2\sqrt{I_s(\mathbf{x}_n, t) I_{\mathrm{LO}}(\mathbf{x}_n)} \cos\left(\omega_{\mathrm{IF}} t + \varphi_s(t) - \varphi_{\mathrm{LO}}(t)\right), \end{aligned} \tag{17}$$

where the intensity of the up-converted RF signal I_s is obtained from:

$$\begin{aligned} U_s(\mathbf{x}, t) &= U_{\mathrm{tot}}(\mathbf{x}) \left[A_s(t) e^{j\varphi_s(t)}\right] e^{j\omega_1 t} \\ &= \sqrt{I_s(\mathbf{x}, t)} e^{j\omega_1 t}. \end{aligned} \tag{18}$$

Above, $A_s(t)e^{j\varphi_s(t)} \equiv S(t)$ represents the baseband modulation of the captured RF signal that we wish to recover at IF. $U_{\text{tot}}(\mathbf{x})$ is the amplitude of the spatial distribution of light after beamforming, derived in (C.6). Examination of (17) shows that the intensity incident on the photodetector is proportional to the RF signal.

Substituting for $U_s(\mathbf{x}, t)$ in (17) using (18) yields

$$I_n(t) = \sqrt{I_{\text{LO}}(\mathbf{x}_n)}U_{\text{tot}}(\mathbf{x}_n)A_s(t)\cos\left(\omega_{\text{IF}}t + \varphi_{\text{IF}}(t)\right), \quad (19)$$

where $\varphi_{\text{IF}}(t) = \varphi_s(t) - \varphi_{\text{LO}}(t)$ is the phase difference between the modulation $S(t)$ and the LO. Finally, we obtain the IF photocurrent from a detector at $\mathbf{x}_n$ as:

$$i_n^{\text{IF}}(t) \propto \mathcal{R}I_n(t) + \text{noise}, \quad (20)$$

where $\mathcal{R}$ is the responsivity (Amperes per Watt) of the photodiode, and 'noise' represents photocurrent from the lasers' relative intensity noise (RIN), upconverted input thermal noise, and shot noise.

Ideally, the LO has constant amplitude and frequency with no additional time-dependent phase, and thus the IF signal replicates the modulation on the received signal ($\phi_{\text{IF}}(t) = \phi_s(t)$). In practice, small perturbations of the fiber conveying the LO to the detector lead to undesired phase noise in the obtained IF signal, but these perturbations are generally slow compared to the time scale of the baseband modulation $S(t)$ and can be easily filtered out.

It should be noted that the expressions above pertain to detection at a single point in the image plane, $\mathbf{x}_n$. Real photodetectors have a finite detection area, and hence (19) must be integrated over the detector area to obtain the correct IF current. Alternatively, the detector in the image plane can be replaced with an optical fiber pick-up, to convey the optical signal to a fiber-coupled photodetector. Such an arrangement alleviates the need for a densely integrated array of detectors in the image plane and enables the use of commercially available fiber-coupled packaged detectors, which are generally far less expensive and have wider bandwidth than integrated near-IR detector arrays. It also allows the LO to be combined with the up-converted signal in a fiber coupler after the pickup, rather than in free space, which provides even greater design flexibility. If a fiber pickup is used, the aforementioned integration over the detector area is replaced by a mode-overlap integration, to account for the limited spatial mode(s) supported by the pickup fiber. In the case of a single-mode fiber, only the component of the image-plane amplitude distribution $U(\mathbf{x})$ that overlaps the fiber mode (approximately Gaussian) is captured and conveyed to the detector. When the magnification of the optical image is well matched to the size and spacing of the pickup fibers, such modal filtering can be useful to improve spatial isolation and reduce crosstalk between detectors corresponding to different resolved spatial beams of the antenna aperture [54].

In addition, due to the comparatively lower IF frequency, as compared to the RF carrier frequency in the transmit case, the photodetector need not be a high-performance device such as was described in Section III-D. Instead, a low-cost photoreceiver with integrated transimpedance amplifier (TIA) may be used, increasing the output signal level, and narrowing the noise bandwidth. Increased transimpedance gain improves the overall SNR up to the point where TIA noise power spectral density (PSD) matches or exceeds other noise contributions (mainly up-converted input thermal noise and shot noise, controlled respectively by LNA gain and LO laser power).

A final consideration in the down-conversion analysis arises from the expression for the LO frequency (16). Because there are two possible values for ω_{LO} that produce the same IF from any given RF input, likewise there are two RF input frequencies that produce the same IF for a given LO. Hence, the condition may arise wherein the recovery of a desired signal at ω_{RF1}, using an LO frequency $\omega_{\text{LO}} = \omega_1 + (\omega_{\text{RF1}} - \omega_{\text{IF}})$, is impaired by interference in the IF output from an undesired signal at ω_{RF2}, where $\omega_{\text{RF2}} = \omega_{\text{RF1}} - 2\omega_{\text{IF}}$. Both RF signals will generate the same IF (apart from a minus sign representing a π phase shift). The undesired signal frequency is called an "image" frequency, due to its symmetric location in the frequency spectrum with respect to the LO (not to be confused with the spatial imaging of RF sources formed by the receiver). This situation is common among wideband electronic receivers, and considerable work has been dedicated to designing and optimizing so-called "image-rejection" schemes, typically based on filters, mixers [55], [56], or combinations thereof. Furthermore, in recent years, as interest in photonics for wideband RF systems has grown, numerous designs have been proposed for photonic image-rejection mixers. An overview can be found in the review article of Zhu and Pan [57]. We have developed solutions that are specifically tailored to this receiver architecture, which are beyond the scope of this paper; further details can be found in [58].

V. MULTI-BAND, MULTI-BEAM TRANSMIT ARCHITECTURE

The transmitter architecture of Fig. 4 may be modified, as in Fig. 6, to simultaneously support multiple bands and multiple simultaneous beams. The multi-band system includes several distinct functional blocks, including several TOPSs for pure RF carrier generation, data-modulation blocks for sector signal feed, a non-blocking optical switch matrix, an optical lens for beam forming, EDFAs for optical amplification, variable optical attenuators (VOAs) for antenna-array apodization, optical feed network, and a photonic RRU that includes photodiodes, power amplifiers and antenna array. The system supports simultaneous multiple bands, multiple users, and multiple beams.

In each TOPS band, the clone-laser arm is split into multiple channels and modulated by an array of I/Q modulators serving separate spatial sectors. In addition to the I/Q modulators, each sector-modulation block includes a pair of driving amplifiers and an EDFA pre-amplifier. The I/Q modulator is biased to suppress carrier and one of the sidebands. As shown

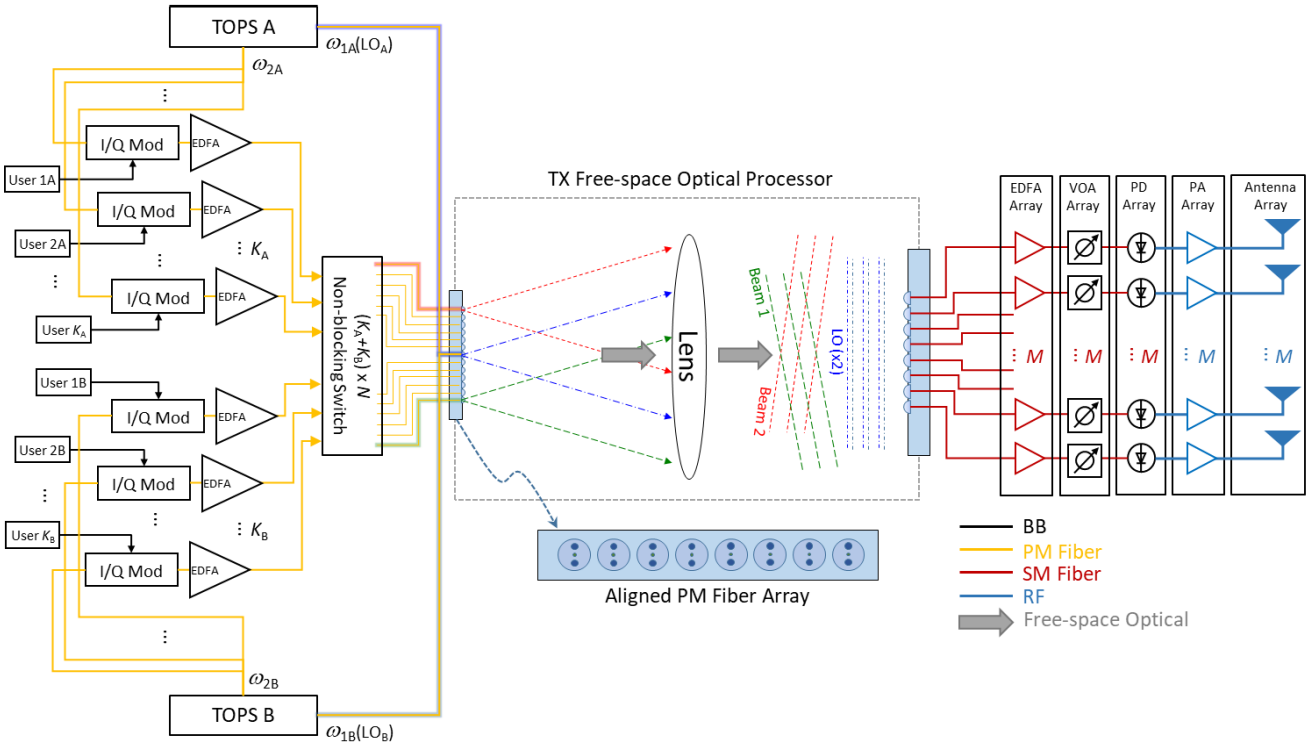

FIGURE 6. Block diagram of a photonically enabled simultaneous multi-band, multi-sector transmit phased-array system using an optical lens as a beamformer.

in Fig. 6, after data modulation, the $K = (K_A + K_B) \leq M$ signals are fed into a $K \times N$ non-blocking optical switch, whose N outputs are routed to a fiber array. This way, the optical switch enables independent, simultaneous routing of every sector-modulation block output to any fiber of the array.

The fiber array is placed in the focal plane of a lens, which collimates the diverging fiber outputs into plane waves, so that the direction of propagation of a plane wave is a function of the fiber position in the array, see Fig. 6. On the far end of the optical system, a pickup fiber array placed in the focal plane of the lens collects the plane waves. Each pickup fiber receives the same optical signal except for the optical phase that depends on the plane-wave direction of propagation. The mapping of the input-fiber position to the plane-wave direction of propagation that yields optical-phase profiles in the light collected by the pickup fibers constitutes beam forming. Multiple beams are formed simultaneously at the same or different optical wavelengths (since the lens-based beamforming is wavelength agnostic).

Meanwhile, optical reference wavelengths from multiple TOPSs are combined and fed to the central fiber of the input fiber array, see Fig. 6. This way, the optical references are evenly distributed with a constant phase across the pickup fiber array. The reference and modulated clone wavelengths are combined in pickup fibers and routed to EDFAs for amplification. The EDFA outputs are fed to high-speed/high-power photodiodes that drive antenna elements. This way, a tunable multi-band, multi-beam, multi-user transmit system is established. If needed, VOAs may be inserted into the system to provide a desired amplitude distribution across the array and achieve optimal array gain pattern. Optionally, RF power amplifiers (PAs) may be used to increase the total radiated power.

The architecture of Fig. 6 offers several advantages over conventional phased arrays. First, it is scalable and relatively straightforward to implement—especially when leveraging emerging chip-level photonic integrated circuit (PIC) techniques. The transmit system supports multiple channels feeding multiple spatial sectors simultaneously and, thanks to the incorporation of an optical switch that can arbitrarily re-route modulator-block outputs to any spatial sectors, offers enhanced signal redundancy and reconfigurability. Furthermore, the system has the potential to increase the radiated power at improved linearity, as the number of spatial sectors, which equals the number of input fibers on the left of the optical system, need not equal the number of pickup fibers on the right. By increasing the number of the latter, optical power may be spread over a larger number of photodetectors, which allows increasing the total optical power, and thereby the total radiated RF power while maintaining or reducing the RF gain of the individual RF power amplifiers serving the antenna array. Benefits of such a fiber-number disparity include enhanced linearity of the transmitted signals in addition to improved redundancy in case of a failure of an amplifier or a transmit antenna since the antenna array would be over-sampled, potentially by a large factor. In the extreme case, the amount of optical power delivered to the (larger number of) photodetectors may be so high as to allow the

elimination of RF power amplifiers, thereby simplifying the system architecture and improving linear performance.

The capability of the proposed architecture to process in parallel multiple beams at the transmitter and at the receiver greatly reduces the issues related to network discovery, cell search, and initial access [59] which become more and more problematic as narrower beams are formed by the BTS and for scenarios where node location is not known *a priori* [28]. Recent simulation-based results confirming initial access latency reductions when the BTS supports multiple beams at the transmit side were recently reported in [48]. Further latency reduction can be expected when parallel processing of receive beams is also supported as in the proposed architecture where the receiver is basically acting as a ''staring array'' across the whole field of view, eliminating the need for beam scanning.

VI. EXPERIMENTAL RESULTS

A. TRANSMITTER ARCHITECTURE

The suitability of photonic transmitter arrays for MU-MIMO was demonstrated in the results found in [34]. In that work, a TOPS source was used to set the carrier frequency, and optical modulation was used to simultaneously encode data and beamform for two simulated users with a 1×2 transmitter array. Beamforming was performed in the digital domain, and user data needed to be encoded for each element of the transmitter array individually. In contrast, the imaging transmitter presented here requires only one data modulator per user, because the data modulation happens in the beam space. Hence, the BBU is concerned only with directing data to the transmit beam that corresponds to one of the N spatial sectors in which the receiving user is located; (analog) element-level phasing happens automatically in the beamspace processor. Notably, pilot and/or data signals from the user equipment, captured by the imaging receiver, automatically and instantaneously provide the needed user location information via the analog beamforming functionality (imaging) of the receiver.

A preliminary experimental demonstration of the imaging transmitter has been performed, using a very low RF carrier frequency of 500 MHz, so that the element-level phases could be captured and verified using a multi-channel oscilloscope. An overview of the results is shown in Fig. 7. A TOPS was set up with a frequency offset of 500 MHz, and the two outputs were connected to fiber input ports of a breadboard optical beamspace processor. The processor was a pair of 16-element polarization-maintaining (PM) fiber arrays positioned in the two focal planes of a lens. The oscilloscope was used to capture IF traces from all 16 output fibers as the positions of the two inputs were changed: to form all 16 possible output beams, one laser (the LO, or ω_2) was kept in a fixed position at the center of the input array, while the other laser (ω_1), which would in practice be modulated with a user's data, was moved across all the input positions. The plots on the right side of (b)-(d) confirm that the slope of the IF phases at the processor output is determined by the position of the ω_1 input fiber. Also note that the correct phases are obtained irrespective of the generated TX carrier frequency, due to the extremely narrow bandwidth of the RF spectrum in comparison to the optical frequencies used, and the fact that both optical frequencies pass through the same beamforming optics prior to down-conversion to RF. Hence, the RF phase at each element is determined entirely by the spatial separation in the input plane between the signal and OLO lasers, and the positions of the pickup fibers feeding each element.

B. RECEIVER ARCHITECTURE

A first-generation 8-element 1D prototype receiver system was presented with experimental characterization and application demonstrations in [53], [60], [61], and [62]. Recently, characterization of a second-generation photonic phased-array receiver system has been performed using a new 1×15 RX system operating over a frequency range of 20-40 GHz, with a modular, swappable RF front-end implementation. Fig. 8(a) depicts the system's front end, comprising the RF front end (antenna plus LNAs) connected to the photonic up-conversion modulator array using SMPM plug-in connectors. The beam pattern, or point-spread function (PSF) for this 15-element array was measured directly in the optical Fourier plane using a short-wave infrared (SWIR) line-scan camera, and is shown in Fig. 8(b), showing very close agreement with an analytically calculated beam pattern.

The results of single-source characterization experiments showed that the overall noise figure (NF) of the receiver array was <10 dB (relative to an ideal beamformer with the same number of elements) for input signals ranging from 21 to 28 GHz, while the minimum NF at 23 GHz was 7 dB. The frequency dependence of the NF largely tracks the gain of the 2-stage front-end LNAs, which varies from a maximum of 47 dB at 23 GHz to 30 dB at 40 GHz. It should be noted that due to their wide bandwidth, the NF of the PCB-integrated LNAs alone was $\sim$5 dB, contributing significantly to the overall system NF. Isolation between spatial sectors was >24 dB, due to the spatial orthogonality of the 15 beams formed by the optical processor. The IF bandwidth was 2.4 GHz, set by the commercial PD-TIA device used to recover the IF signals.

In a recent technical paper [63], the beamforming capabilities of all-electronic systems with analog, hybrid, and digital beamforming architectures were compared by Analog Devices using two metrics: the usual BBP (Hz) and the beamforming power efficiency or power consumption per BBP (W/Hz). The result of this comparison puts achievable BBPs in the range of 0.5–4 GHz for digital/hybrid beamforming and 0.6–2.5 GHz for analog beamforming.[2] For comparison, the BBP goal set by DARPA for Phase 2 of

[2]These values can be obtained combining the results of Figures 4 and 5 of [63]. We also point out that, for digital beamforming, the author of [63] has assumed that, once the maximum DSP capacity is reached, the power consumption does not increase anymore. Thus, beyond that point, bandwidth per beam is reduced for an increasing number of beams. This necessary tradeoff between the number of simultaneous beams and the bandwidth per beam has also been acknowledged by DARPA [28]. This tradeoff is not present in opto-electronic architectures like the one proposed here.

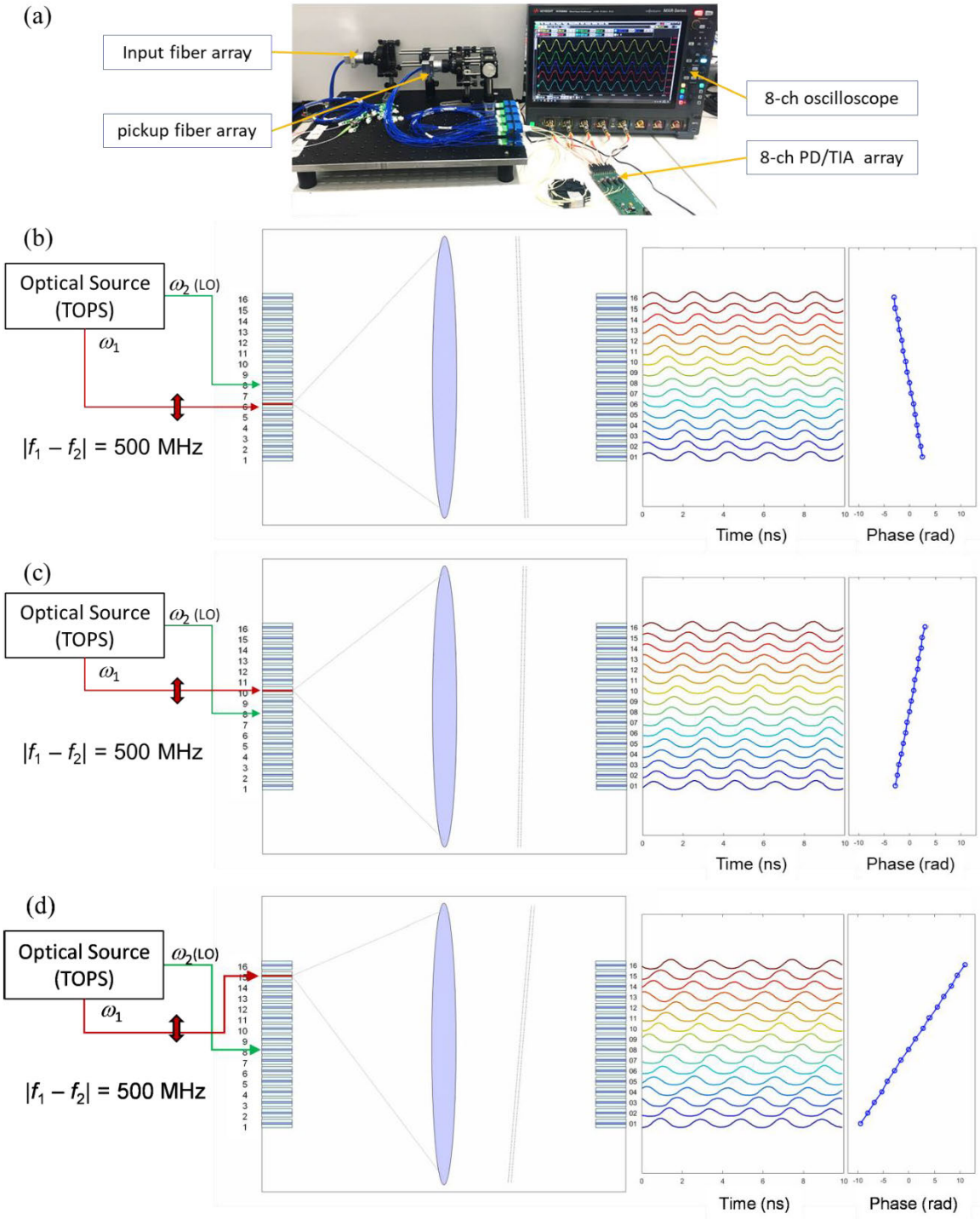

FIGURE 7. Imaging transmitter beamforming demonstration experiment. (a) Experimental setup comprising optical fiber arrays in the focal planes of the FT lens, along with a PD array and multichannel oscilloscope. (The TOPS is not shown.) IF traces were captured from all 16 output channels using a common trigger when the TOPS output ω_1 was inserted into each of 16 inputs; ω_2 was kept in a constant, centered position. IF traces and extracted phase profiles are shown in (b)-(d) for three input positions, showing that the tilted phase profile required for beamforming is indeed obtained when these IFs are fed to the PDs corresponding to antenna array elements.

its MIDAS program is at least 3.2 GHz using digital beamforming [28]. With 2.4 GHz of IF bandwidth in each beam, and 15 beams formed simultaneously and continuously, the system proposed in this paper has a nominal BBP of 36 GHz

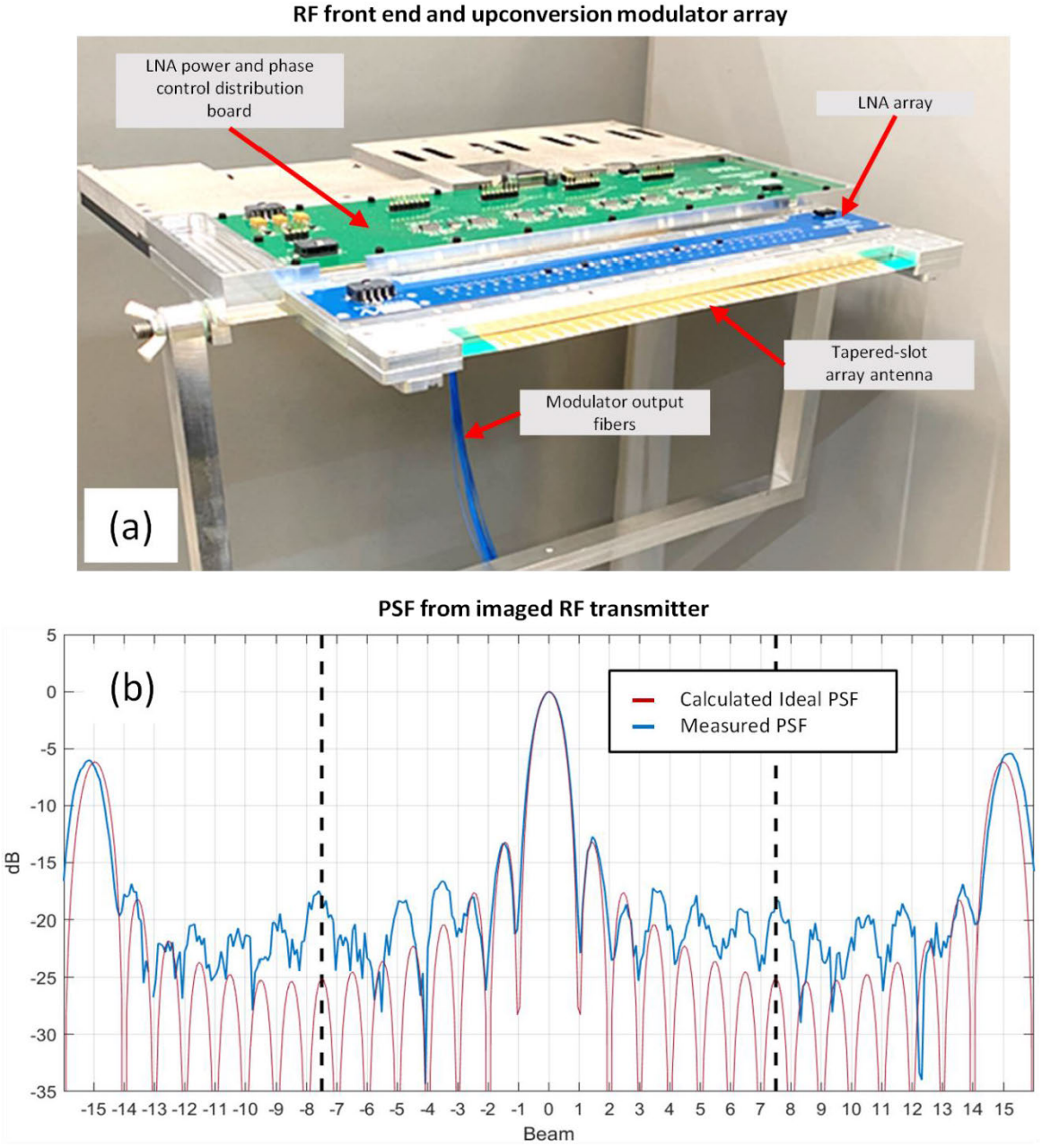

FIGURE 8. (a) Photograph of the 15-channel photonic imaging receiver system's front end, comprising an array of tapered-slot antennas, behind which are two stages of LNA gain (blue board), feeding an array of optical modulators (beneath the green power-distribution/phase-control board). Although the housing and boards have spaces for 32 elements only the center 15 elements are populated with LNAs and modulators. (b) Measured system response from a boresighted RF source, a.k.a., the point spread function (PSF) of the array, as captured by a near-infrared line-scan camera (blue trace). Also plotted for comparison is a calculated ideal PSF for a 15-element array (red trace). Vertical dashed lines indicate the alias-free region of the image, containing 15 resolved beams. The beams in the optical image plane are separated by 0.25 mm, corresponding to the spacing of the optical fibers in the fiber pickup array that feeds the IF detectors.

which is an order of magnitude higher than what is considered achievable with all-electronic implementations. The proposed architecture performs very well also in terms of BBP power efficiency. In the Analog Devices report, state-of-the-art all-electronic beamforming systems capable of supporting 15 beams are estimated to have power efficiencies of 210 and 50 W/GHz for digital and analog/hybrid systems, respectively (see Figure 5 in [63]). The total power consumed by the proposed system is under 300 W, which includes a standard PC/monitor, while key subsystems were individually measured to consume only 120 W. Using the former figure's more conservative power estimate, this yields

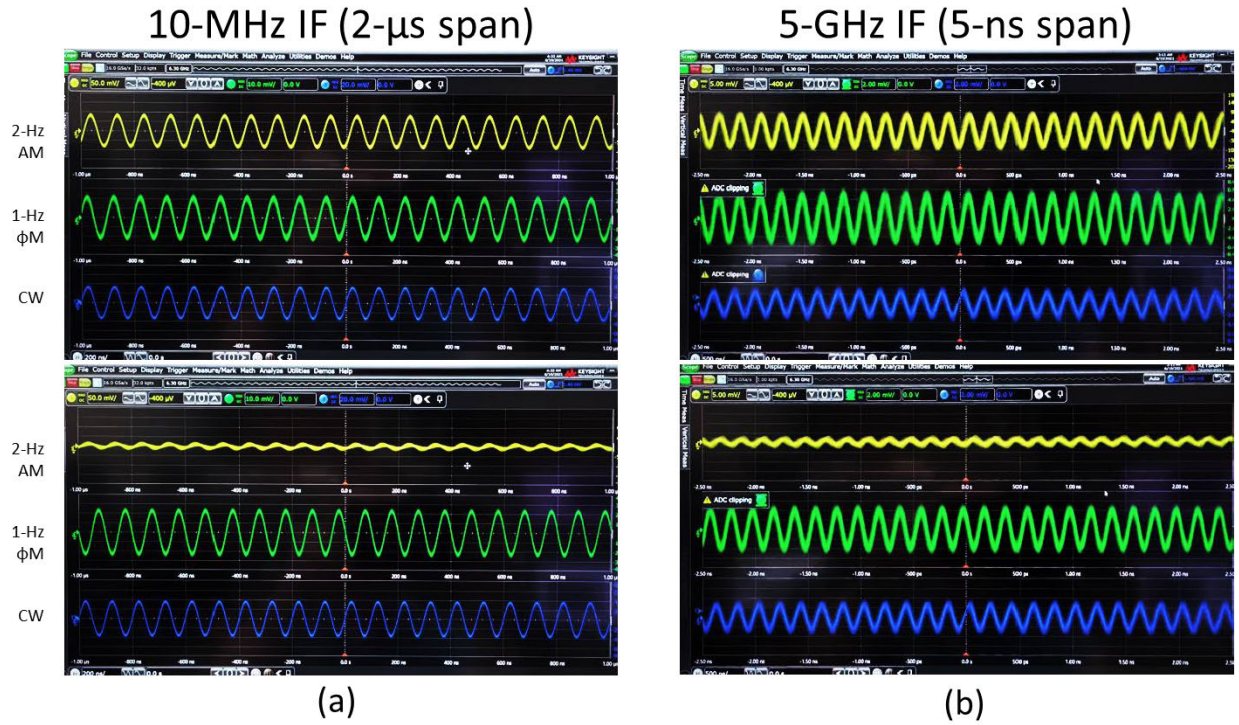

FIGURE 9. Oscilloscope screen captures showing the receiver system's simultaneous IF signal recovery of three separate sources over a 5-GHz IF range. Each source corresponds to a different color trace in each image: yellow = amplitude modulation (AM), green = phase modulation (ΦM), blue = continuous-wave (CW). Top row and bottom row are for identical receiver configurations, with images captured at different times to illustrate the AM on the yellow trace (top row at maximum amplitude, bottom at minimum) and ΦM on the green trace (pi phase shift between top and bottom, where the reference phase was obtained from oscilloscope triggering on the blue CW trace). The IFs were tuned to (a) 10 MHz and (b) 5 GHz, and similar traces were observed over the entire IF range in between.

a beamforming power efficiency of only 8 W/GHz which is at least 6× lower than what is considered achievable with all-electronic implementations.

While it was impractical to experimentally demonstrate the operation of this system at its full BBP capacity, which would require 15 microwave signal generators, we have experimentally demonstrated extremely high BBP using three simultaneous sources. In the first demonstration, three signal generators were set up transmitting at 26.5 GHz with roughly equal power, aligned to three separate beams of the antenna array. To distinguish among the received signals at IF when observed on an oscilloscope, each was time modulated in a different manner: (1) 2-Hz amplitude modulation (AM); (2) 1-Hz phase modulation (ΦM), and continuous-wave (CW). To demonstrate signal recovery over a wide IF bandwidth, the optical LO was tuned to yield IF outputs from 10 MHz up to 5 GHz. Although the 5-GHz IF exceeds the nominal 3-dB-rolloff bandwidth of the PD-TIAs, the response was still strong enough to be measured over this entire IF range. Moreover, PD-TIAs with up to 10 GHz of bandwidth are available commercially, so it is reasonable to assert that our photonic receiver can provide at least 10 GHz of bandwidth per beam thus reaching a potential BBP of 150 GHz. Showing simultaneous 3-beam IF recovery over 5 GHz of continuous IF bandwidth, we obtain a demonstrated BBP of 15 GHz which is still much higher than what is considered achievable today with all-electronic implementations. This result is summarized in Fig. 9.

Additionally, to demonstrate the ability of the system to recover wideband digital communications waveforms with high fidelity, an additional multi-beam experiment was performed [64]. In this demonstration, three RF signal generators were once again set up to transmit, all at the same frequency of 27 GHz. TX antennas were positioned in three separate spatial beams: beams 6, 8 and 9 of the array's 15 beams, as shown in the diagram of Fig. 10(a) and the photograph of Fig. 10(b). Different modulations were applied to the three sources: one source was CW, one was modulated at 300 Mbaud with 32APSK pseudo-random bit sequency (PRBS) data (1.5 Gbps), and one was modulated at 1 Gbaud with 16QAM PRBS data (4 Gbps). Due to the orthogonality of the beams, all three signals could be recovered at IF simultaneously with good fidelity and isolation, despite all signals having the same carrier frequency. This can be seen in Fig. 10(c), which shows constellations and IF spectra obtained simultaneously from all three sources. Measured EVM was 4.5% for the 32APSK signal, and 6% for the 16QAM.

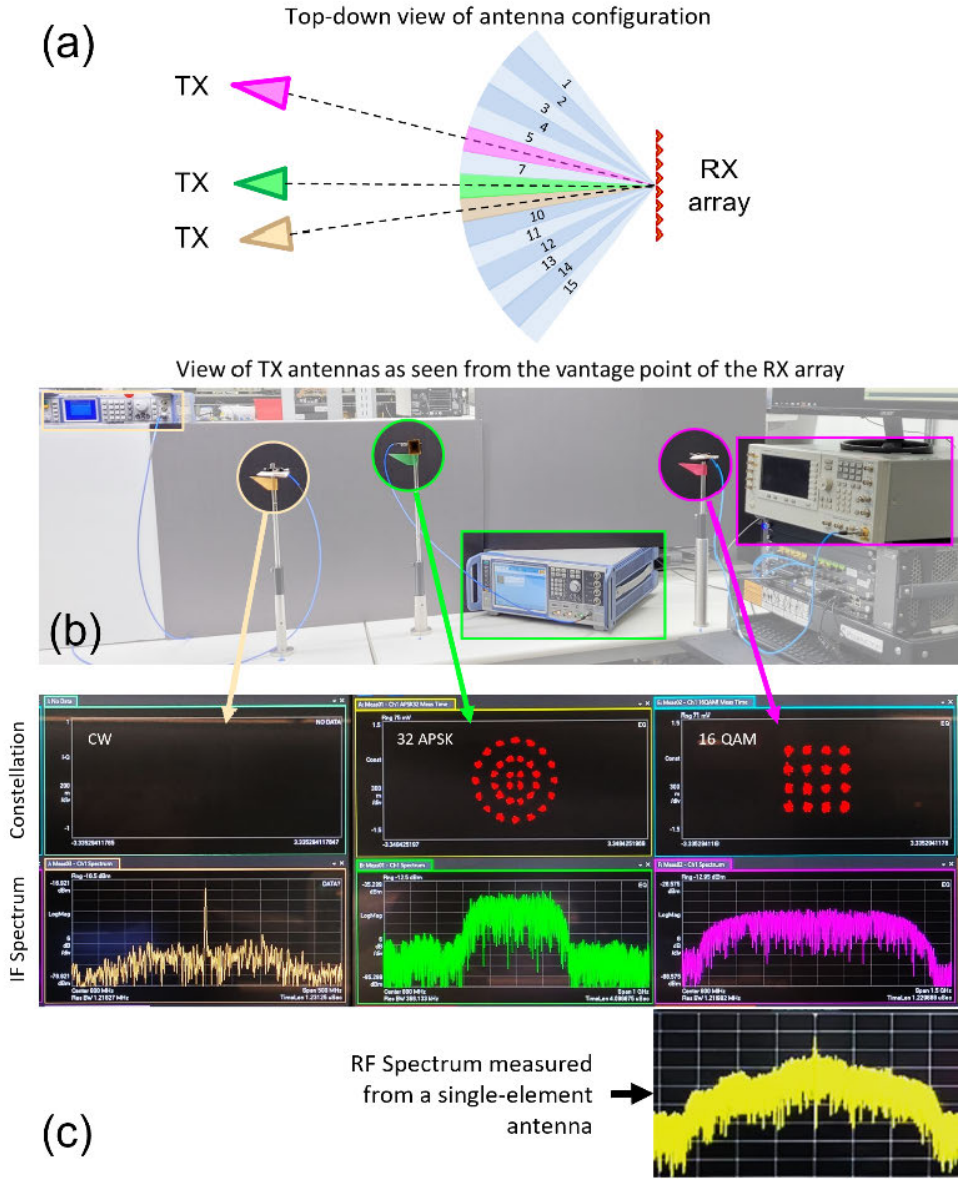

FIGURE 10. (a) Diagram of the TX and RX antenna configuration for imaging receiver demonstration experiment. All 3 TX sources were transmitting at the same frequency, 27 GHz. (b) Photograph of the antenna configuration. Antenna mounts are labeled with colors to match the colors of the diagram in (a). (c) Screen capture of vector signal analysis software running on a multichannel oscilloscope showing simultaneous spectra from spatially separated IF output channels. Top row: demodulated data constellations (2 of the 3 sources carried data, the leftmost source was CW). Middle row: IF signal spectra showing signal bandwidths of 0 Hz (CW), 300 MHz, and 1 GHz, from each source left to right, respectively (all spectrum plots have 1.5-GHz span, centered at 800 MHz, and 10 dB/div). At bottom is the spectrum from a separate single-element antenna, showing the interference of the 3 simultaneous signals without the receiver's optical beamforming (1.5-GHz span centered at 27 GHz, 10 dB/div).

Figure 10(c) also shows a spectrum obtained at the same time from a single-element receiver, showing the spectra of all three signals overlaid upon one another. A conventional all-electronic receiver, e.g., a digital beamformer, would need to sample at a high rate the signal from each individual antenna and use computationally intensive processing to spatially separate these signals, which incurs significant performance penalties in terms of fidelity, latency, and especially power consumption. In contrast, our system performs all the beamforming in the optical, analog domain, with zero power consumption, at the speed of light, thereby allowing the DSP hardware to be optimized for IF/BB signal recovery.

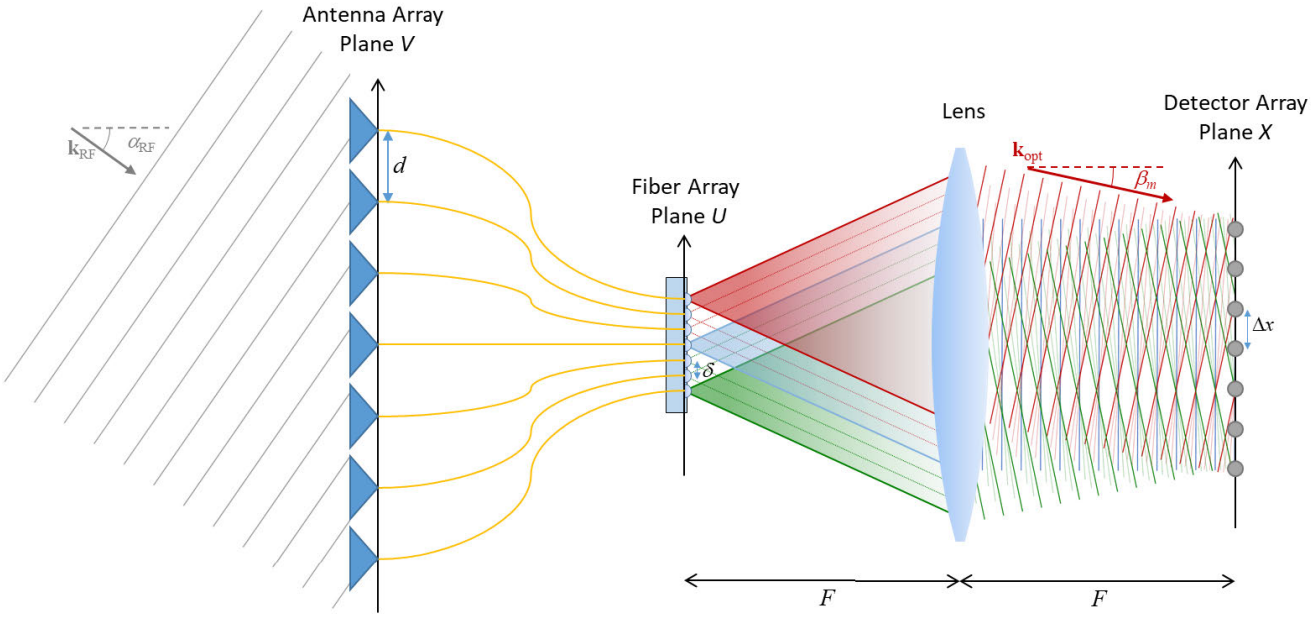

FIGURE 11. Configuration of a lens-based approach to RF receive beamforming.

VII. SUMMARY

Novel transmit and receive phased-array architectures have been presented, based on high-performance RF-photonic devices for coherent up-conversion and down-conversion. Techniques for preserving spatial and temporal coherence in the optical domain have been developed that enable the use of optical components for RF beamforming and signal modulation. Notably, passive, all-optical beamforming performed by a simple lens offers virtually unlimited BBP with speed-of-light latency, while significantly reducing the number of required components in the RRU.

For transmit systems, spatial coherence is achieved by routing frequency-offset optical signals in the same fibers, cancelling any fiber-induced phase perturbations. In receive systems, a closed-loop feedback scheme monitors and actively compensates for perturbations in real time. Temporal coherence is obtained through the use of a common laser to feed all array elements and is preserved for optical heterodyne mixing processes by a modulation-sideband injection locking scheme for widely tunable OLO generation.

The presented architectures cover both analog and fully connected hybrid beamforming implementations and address numerous challenges facing the practical implementation of envisioned next-generation M-MIMO wireless communications systems. They are more flexible than their all-electronic counterparts and can support extremely high BBPs even with mere analog beamforming. They provide wide bandwidth, multi-beam, and multi-band capabilities while simplifying deployments and reducing life-cycle management costs, since a common optical baseband and beamforming engine can be connected to swappable band-specific antennas and amplifiers.

Ongoing work promises to implement these architectures in highly scalable chip-based form factors by leveraging recent developments in PIC-based design, fabrication, and integration [64].

APPENDIX

A. CONVENTIONS

Ignoring polarization, an optical wave may be described mathematically by a real-valued function $u(\mathbf{r}, t)$ of position $\mathbf{r} = (x, y, z)$ and time t that satisfies the wave equation:

$$\nabla^2 u(\mathbf{r}, t) = \frac{\partial^2 u(\mathbf{r}, t)}{\partial t^2}. \tag{A.1}$$

The real-valued function $u(\mathbf{r}, t)$ is known as the *scalar wavefunction*. For nearly monochromatic waves, it is often convenient to express $u(\mathbf{r}, t)$ as the real part (denoted by $\Re$) of a *complex wavefunction* $U(\mathbf{r}, t)$, and to separate the fast oscillations at optical frequency ω from the slowly-varying complex envelope $\zeta(\mathbf{r}, t) = a(\mathbf{r}, t)e^{j\varphi(\mathbf{r},t)}$ $[a, \varphi \in \mathbb{R}]$ so that:

$$u(\mathbf{r}, t) = \Re\left[U(\mathbf{r}, t)\right], \text{ with} \tag{A.2}$$

$$U(\mathbf{r}, t) = \zeta(\mathbf{r}, t)e^{j(\mathbf{k}\cdot\mathbf{r}-\omega t)} = a(\mathbf{r}, t)e^{j\varphi(\mathbf{r},t)}e^{j(\mathbf{k}\cdot\mathbf{r}-\omega t)}. \tag{A.3}$$

Such formulation simplifies the description of interference effects between nearly monochromatic waves oscillating at neighboring optical frequencies.

The optical intensity $I(\mathbf{r}, t)$ of a wave described by $u(\mathbf{r}, t)$ is the time-average square of $u(\mathbf{r}, t)$, where averaging is understood to be taking place over time periods that are long compared to the optical oscillation period $2\pi/\omega$, but short compared to the temporal variability of $\zeta(\mathbf{r}, t)$.

With (A.2), $I(\mathbf{r}, t)$ becomes:

$$\begin{aligned} I(\mathbf{r}, t) &= 2\left\langle u^2(\mathbf{r}, t)\right\rangle \\ &= \left\langle |U(\mathbf{r}, t)|^2\right\rangle \\ &= 2\left\langle a^2(\mathbf{r}, t)\cos^2\left(\omega t - \mathbf{k}\cdot\mathbf{r} + \varphi(\mathbf{r}, t)\right)\right\rangle \\ &= |\zeta(\mathbf{r}, t)|^2 \left\langle 1 + \cos\left(2\omega t - 2\mathbf{k}\cdot\mathbf{r} + 2\varphi(\mathbf{r}, t)\right)\right\rangle \\ &= |\zeta(\mathbf{r}, t)|^2, \end{aligned} \tag{A.4}$$

where the factor of 2 in the first line of (A.4) is used for convenient scaling of the subsequent expressions. Note that (A.4) implicitly defines the units of the scalar wavefunction: u is proportional to the electric field amplitude E, and effectively equivalent within a factor of the proportionality constant (the wave impedance of the propagation medium). The optical power of the wave is defined in such convention as:

$$P = \tfrac{1}{2}\int I \, \mathrm{d}A, \tag{A.5}$$

where the integration is over the area of a plane transverse to the direction of propagation. Power and intensity are often effectively interchangeable when discussing optical signals that are laterally confined, such as in optical fibers. For plane waves in free space, which have uniform intensity, power is simply the product of the intensity and the detector area.

Using (A.4), the complex envelope $\zeta(\mathbf{r}, t)$ may also be expressed as:

$$\zeta(\mathbf{r}, t) = a(\mathbf{r}, t)e^{j\varphi(\mathbf{r},t)} = \sqrt{I(\mathbf{r}, t)}e^{j\varphi(\mathbf{r},t)}. \tag{A.6}$$

B. COHERENT PHOTOMIXING

Let us consider two waves with scalar wavefunctions $u_1(\mathbf{r}, t)$ and $u_2(\mathbf{r}, t)$ that are superimposed with each other, interfering. Linearity of the wave equation (A.1) implies superposition of effects, so that the total wavefunction is the sum of the individual wavefunctions:

$$\begin{aligned} u(\mathbf{r}, t) &= u_1(\mathbf{r}, t) + u_2(\mathbf{r}, t), \\ U(\mathbf{r}, t) &= U_1(\mathbf{r}, t) + U_2(\mathbf{r}, t). \end{aligned} \tag{B.1}$$

Let us now consider the two nearly monochromatic optical waves described by:

$$U_1(\mathbf{r}, t) = \sqrt{I_1(\mathbf{r}, t)}e^{j\varphi_1(\mathbf{r},t)}e^{j\omega_1 t} \tag{B.2}$$

$$U_2(\mathbf{r}, t) = \sqrt{I_2(\mathbf{r}, t)}e^{j\varphi_2(\mathbf{r},t)}e^{j\omega_2 t}. \tag{B.3}$$

The intensity of the superposition of these two waves is given by:

$$\begin{aligned} I(\mathbf{r}, t) &= \left\langle |U(\mathbf{r}, t)|^2\right\rangle = \left\langle |U_1(\mathbf{r}, t) + U_2(\mathbf{r}, t)|^2\right\rangle \\ &= I_1(\mathbf{r}, t) + I_2(\mathbf{r}, t) + 2\left\langle \Re\left[U_1(\mathbf{r}, t)U_2^*(\mathbf{r}, t)\right]\right\rangle \\ &= I_1(\mathbf{r}, t) + I_2(\mathbf{r}, t) \\ &\quad + 2\sqrt{I_1(\mathbf{r}, t)I_2(\mathbf{r}, t)}\cos\left(\omega_{\mathrm{RF}} t + \Delta\varphi(\mathbf{r}, t)\right), \end{aligned} \tag{B.4}$$

where U^* denotes the complex conjugate of U, $\omega_{\mathrm{RF}} = \omega_1 - \omega_2$, $\Delta\varphi(\mathbf{r}, t) = \varphi_1(\mathbf{r}, t) - \varphi_2(\mathbf{r}, t)$, and the last expression is obtained when $\omega_{\mathrm{RF}} \ll \omega_1 + \omega_2$. For balanced beams $I_1(\mathbf{r}, t) = I_2(\mathbf{r}, t) \equiv I_0(\mathbf{r}, t)$, (B.4) simplifies to:

$$I(\mathbf{r}, t) = 2I_0(\mathbf{r}, t)\left[1 + \cos\left(\omega_{\mathrm{RF}} + \Delta\varphi(\mathbf{r}, t)\right)\right]. \tag{B.5}$$

Photodetectors sense optical power, i.e., the intensity integrated over the detector area, producing an output current proportional to the input optical power. This current oscillates at the difference frequency ω_{RF} as long as it is within the detectors' response bandwidth.

C. RECEIVE BEAMFORMING

Fig. 11 shows a simple configuration for RF receiver beamforming in a hybrid O/E architecture. Let us consider an incoming RF plane wave characterized by wavevector $\mathbf{k}_{\mathrm{RF}}$, propagating at an angle α_{RF} with respect to the normal of the antenna array plane V of coordinates $\mathbf{v} = (x_v, y_v)$. The signal received by the m^{th} antenna of an M-antenna uniform linear array ($m = 0, 1, \ldots, M-1$) can be expressed as:

$$\begin{aligned} U_m^{\mathrm{RF}}(\mathbf{v}_m) &= U_0^{\mathrm{RF}} e^{-j\mathbf{k}_{\mathrm{RF}}\cdot\mathbf{v}_m} \\ &\equiv U_0^{\mathrm{RF}} e^{-j\theta_m}, \end{aligned} \tag{C.1}$$

where U_0^{RF} is the complex amplitude of the received signal, and θ_m is the phase of the RF plane wave sensed by the m^{th} antenna, given by:

$$\theta_m = \mathbf{k}_{\mathrm{RF}}\cdot\mathbf{v}_m = \frac{2\pi}{\lambda_{\mathrm{RF}}} md\sin(\alpha_{\mathrm{RF}}). \tag{C.2}$$

Here, λ_{RF} is the RF carrier wavelength, and d is the antenna spacing, hence the position of the antenna in plane V is $\mathbf{v}_m = (0, md)$.

Behind the antennas, the RF wave is up-converted to the optical domain by electro-optic modulators, an operation that preserves the phase relations (C.2) among the M channels. The up-converted signals $U_m^{\mathrm{opt}} \propto U_m^{\mathrm{RF}}$ propagate in optical fibers that terminate at a fiber array in plane U positioned one focal length F away from the lens, as shown in Fig. 11. The distance between adjacent fiber terminations in the fiber array is δ.

If we model the open fiber terminations on plane U as point sources, we then have M diverging spherical waves that propagate through free space toward the lens and, after passing the lens, continue as collimated plane waves toward the photodetector array located at plane X. Plane X, like plane U, is located one focal length F from the lens. The array of S detectors (or pickup fibers) is located in plane X and the spacing between the photodetectors is Δx. The M collimated plane waves propagate in directions β_m whose values depend on the displacement $m\delta$ of the position of the m^{th} fiber termination from the lens axis:

$$m\delta = F\tan(\beta_m) \approx F\beta_m, \tag{C.3}$$

where the paraxial (small-angle) approximation was used to obtain the right-hand expression. This approximation is well satisfied so long as the focal length is much larger than the fiber/detector positions, i.e., $F \gg M\delta$, $F \gg S\Delta x$.

The complex amplitude of the m^{th} plane wave incident on the n^{th} photodetector located at position in plane X given by $\mathbf{x}_n = (0, n\Delta x)$ can then be expressed as:

$$\begin{aligned} U_m^{\text{opt}}(\mathbf{x}_n) &= U_0^{\text{opt}} e^{-j(\mathbf{k}_{\text{opt}}\cdot\mathbf{x}_n+\theta_m)} \\ &= U_0^{\text{opt}} e^{-j(\phi_{m,n}+\theta_m)}, \end{aligned} \tag{C.4}$$

where we can see that the optical signal picks up a new phase $\phi_{m,n}$ that adds on top of the RF phase θ_m given in (C.2). This additional phase is given by:

$$\begin{aligned} \phi_{m,n} &= \mathbf{k}_{\text{opt}} \cdot \mathbf{x}_n \\ &= \frac{2\pi}{\lambda_{\text{opt}}} n\Delta x \sin(\beta_m) \\ &\approx \frac{2\pi}{\lambda_{\text{opt}}} n\Delta x \frac{m\delta}{F}, \end{aligned} \tag{C.5}$$

where λ_{opt} is the wavelength of the optical signal and the expression was obtained under the paraxial approximation.

The expression for the total field impinging over the n^{th} photodetector is the superposition of the fields of the M collimated plane waves in (C.4), calculated at position $\mathbf{x}_n$ in the X plane as:

$$\begin{aligned} U_{\text{tot}}^{\text{opt}}(\mathbf{x}_n) &= \sum_{m=0}^{M-1} U_m^{\text{opt}}(\mathbf{x}_n) \\ &= U_0^{\text{opt}} \sum_{m=0}^{M-1} e^{-j(\phi_{m,n}+\theta_m)}. \end{aligned} \tag{C.6}$$

All terms in the sum (C.6) have the same magnitude but may differ in phase, i.e., all lie on a circle in the complex plane. Under the condition:

$$\phi_{m,n} + \theta_m = 2\pi m \left[\frac{(n\Delta x)\,\delta}{\lambda_{\text{opt}} F} + \frac{d}{\lambda_{\text{RF}}} \sin(\alpha_{\text{RF}}) \right] = 0, \tag{C.7}$$

all the terms under summation are equal and add coherently to the value MU_0^{opt}. Hence, a signal arriving to the antenna array at angle α_{RF} produces peak light intensity at the position $(0, n\Delta x)$ of the photodetector plane X satisfying:

$$\begin{aligned} n\Delta x &= -F \left(\frac{d}{\delta}\right) \left(\frac{\lambda_{\text{opt}}}{\lambda_{\text{RF}}}\right) \sin(\alpha_{\text{RF}}) \\ &\equiv -F \eta_g \eta_w \sin(\alpha_{\text{RF}}), \end{aligned} \tag{C.8}$$

where the constant $\eta_g = d/\delta$ depends on geometrical terms that are fixed in a given system, while the quantity $\eta_w = \lambda_{\text{opt}}/\lambda_{\text{RF}}$ depends on the wavelength of the incoming RF wave and thus may change. For any other position $x \neq n\Delta x$ on the X plane, the terms under summation in (C.6) do not add coherently and are distributed around the circle in the complex plane.

Expression (C.8) provides a condition for determining the position in the X plane of the photodetector that will be responsible for down-converting the up-converted RF waves arriving at the antenna array at a given angle. The position for placement of the n^{th} photodetector is the same as the position where the optical field of an up-converted incoming RF waveform arriving at an angle α_{RF} is maximized.

The angular position α_{opt} of the peak light intensity is given by:

$$\tan(\alpha_{\text{opt}}) = \left(\frac{n\Delta x}{F}\right). \tag{C.9}$$

The image magnification may be defined as the ratio of the sine[3] of the angle of the image plane maximum α_{opt} to the sine of the RF angle of incidence α_{RF}, also obtained from (C.8) (in the small-angle approximation) as:

$$\begin{aligned} \frac{\sin(\alpha_{\text{opt}})}{\sin(\alpha_{\text{RF}})} &= \sin\left[\tan^{-1}\left(\frac{n\Delta x}{F}\right)\right] \Big/ \sin(\alpha_{\text{RF}}) \\ &\approx \frac{n\Delta x}{F \sin(\alpha_{\text{RF}})} = -\eta_g \eta_w. \end{aligned} \tag{C.10}$$

The factor $\eta_g \eta_w$ is thus shown to be the angular (de)magnification of the image of the RF scene produced at the detector plane, and the minus sign signifies image inversion. The image inversion is consistent with the observation that the optical field distribution at the detector plane may be expressed as the composition of two Fourier transforms operating on the field of the distant sources comprising the RF scene, and that the composition of two Fourier transforms returns the original function, subject to point reflection with respect to the origin.

The optical wavelength λ_{opt} represents the wavelength of the sideband induced by the modulation process and depends on the wavelength of the incident RF wave λ_{RF}. However, the variation of λ_{opt} as a function of λ_{RF} is extremely small. For example, if the frequency of the RF wave is 100 GHz, the deviation of the corresponding sideband from an optical carrier at 1550 nm is only 0.05%. As a result, the wavelength of the sideband can be assumed to be equal to that of the optical carrier used in the up-conversion process, and variation of the optical wavelength as a function of the detected RF wavelength may be safely disregarded in the scaling factor. On the other hand, the direct effect of RF-wavelength variation on the scaling factor may be significant for broadband systems. For example, a system operating over an octave of bandwidth may introduce scales differing by as much as a factor of two for RF sources operating at the limits of the frequency band. It must be emphasized, however, that the scaling impacts only the spread in the range of incidence angles for RF waves that map onto the detector positions. It does not affect the size or spacing of resolved optical peaks formed in the X plane. The latter is determined solely by the optical wavelength and the maximum input fiber spacing $M\delta$, i.e., the optical aperture, which is a scaled replica of the RF aperture (antenna array).

A related caveat should be mentioned regarding the formation of optical grating lobes in the image plane. In (C.7), we found the condition for peak formation as when the phase factors in (C.6) are equal to unity, i.e., when the arguments

[3]Defining magnification in terms of the sine compensates for the angle-dependent resolution of the aperture, so that the magnification thus defined is independent of RF incidence angle.

of the exponentials are zero. However, the peak condition is also satisfied if all the arguments are integer multiples of 2π. Hence, optical grating lobes will form at positions separated by $F(\lambda_{opt}/\delta)$ in the image plane, or equivalently, at angular intervals of λ_{opt}/δ (paraxial approximation). These optical grating lobes are a result of the under-sampling of the optical aperture that re-transmits the up-converted RF input beam and are not connected to grating lobes of the antenna array, should any exist (i.e., should the antenna array spacing be greater than $\lambda_{RF}/2$). The impact of the optical grating lobes is to diminish the beamforming efficiency, since the fraction of the up-converted signal that forms them is lost to the detector that captures the optical "main lobe." In practice, this loss is minimized by limiting the angular spread of the optical transmit elements, i.e., the fiber inputs to the optical beamformer. Whereas in the preceding discussion we assumed for simplicity that the fibers acted as point sources, in reality each fiber provides a diverging Gaussian beam, which divergence can be further reduced through the use of microlenses, such that the FT of the reduced-divergence Gaussian is matched to the optical grating lobe spacing. In this way, the signal power lost to optical grating lobes is minimized.

ACKNOWLEDGMENT

Dr. Galli's contributions predate his employment with Peraton Laboratories.

REFERENCES

[1] W. Lei, *5G System Design: An End to End Perspective*, 2nd ed. Cham, Switzerland: Springer, 2021.

[2] Y. Xing and T. S. Rappaport, "Propagation measurement system and approach at 140 GHz-moving to 6G and above 100 GHz," in *Proc. IEEE Global Commun. Conf. (GLOBECOM)*, Dec. 2018, pp. 1–6, doi: 10.1109/GLOCOM.2018.8647921.

[3] J. G. Andrews, S. Buzzi, W. Choi, S. V. Hanly, A. Lozano, A. C. K. Soong, and J. C. Zhang, "What will 5G be?" *IEEE J. Sel. Areas Commun.*, vol. 32, no. 6, pp. 1065–1082, Jun. 2014, doi: 10.1109/JSAC.2014.2328098.

[4] T. L. Marzetta, "Noncooperative cellular wireless with unlimited numbers of base station antennas," *IEEE Trans. Wireless Commun.*, vol. 9, no. 11, pp. 3590–3600, Nov. 2010, doi: 10.1109/TWC.2010.092810.091092.

[5] D. W. Prather. (2016). *5G Moves Into the Light: Holographic Massive MIMO*. IEEEE ComSoc Technology News. Accessed: Apr. 29, 2022. [Online]. Available: https://www.comsoc.org/publications/ctn/5g-moves-light-holographic-massive-mimo

[6] H. Yang and T. L. Marzetta, "Performance of conjugate and zero-forcing beamforming in large-scale antenna systems," *IEEE J. Sel. Areas Commun.*, vol. 31, no. 2, pp. 172–179, Feb. 2013, doi: 10.1109/JSAC.2013.130206.

[7] H. Q. Ngo, E. G. Larsson, and T. L. Marzetta, "Energy and spectral efficiency of very large multiuser MIMO systems," *IEEE Trans. Commun.*, vol. 61, no. 4, pp. 1436–1449, Apr. 2013, doi: 10.1109/TCOMM.2013.020413.110848.

[8] E. Björnson, M. Matthaiou, and M. Debbah, "Massive MIMO with non-ideal arbitrary arrays: Hardware scaling laws and circuit-aware design," *IEEE Trans. Wireless Commun.*, vol. 14, no. 8, pp. 4353–4368, Apr. 2015, doi: 10.1109/TWC.2015.2420095.

[9] A. M. Shteiman, S. Galli, L. Mailaender, and X. F. Qi, "The effect of diversity combining on ISI in massive MIMO," in *Proc. IEEE 88th Veh. Technol. Conf. (VTC-Fall)*, Chicago, IL, USA, Aug. 2018, pp. 1–6, doi: 10.1109/VTCFall.2018.8691003.

[10] A. S. Y. Poon and M. Taghivand, "Supporting and enabling circuits for antenna arrays in wireless communications," *Proc. IEEE*, vol. 100, no. 7, pp. 2207–2218, Jul. 2012, doi: 10.1109/JPROC.2012.2186949.

[11] Y. Gao, A. Wen, W. Jiang, Y. Fan, Y. He, and D. Zhou, "Fundamental/subharmonic photonic microwave I/Q up-converter for single sideband and vector signal generation," *IEEE Trans. Microw. Theory Techn.*, vol. 66, no. 9, pp. 4282–4292, Sep. 2018, doi: 10.1109/TMTT.2018.2842722.

[12] A. Satari. (Jan. 29, 2020). *Intelligence Brief: What Will Drive Open RAN in 2020?*. Mobile World Live. Accessed: Apr. 29, 2022. [Online]. Available: https://www.mobileworldlive.com/blog/intelligence-brief-what-will-drive-open-ran-in-2020

[13] A. J. Seeds, M. J. Fice, K. Balakier, M. Natrella, O. Mitrofanov, M. Lamponi, M. Chtioui, F. van Dijk, M. Pepper, G. Aeppli, A. G. Davies, P. Dean, E. Linfield, and C. C. Renaud, "Coherent terahertz photonics," *Opt. Exp.*, vol. 21, no. 19, p. 22988, Sep. 2013, doi: 10.1364/OE.21.022988.

[14] V. J. Urick, J. D. McKinney, and K. J. Williams, *Fundamentals of Microwave Photonics*. Hoboken, NJ, USA: Wiley, 2015.

[15] D. Marpaung, J. Yao, and J. Capmany, "Integrated microwave photonics," *Nature Photon.*, vol. 13, no. 2, pp. 80–90, Feb. 2019, doi: 10.1038/s41566-018-0310-5.

[16] J. Capmany and D. Novak, "Microwave photonics combines two worlds," *Nature Photon.*, vol. 1, no. 6, pp. 319–330, Jun. 2007, doi: 10.1038/nphoton.2007.89.

[17] R. A. Minasian, "Ultra-wideband and adaptive photonic signal processing of microwave signals," *IEEE J. Quantum Electron.*, vol. 52, no. 1, pp. 1–13, Jan. 2016, doi: 10.1109/JQE.2015.2499729.

[18] T. R. Clark and R. Waterhouse, "Photonics for RF front ends," *IEEE Microw. Mag.*, vol. 12, no. 3, pp. 87–95, May 2011, doi: 10.1109/MMM.2011.940319.

[19] C. A. Schuetz, R. D. Martin, D. W. Prather, and T. E. Dillon, "Method for controlling the phase of optical carriers in millimeter wave imaging systems using optical upconversion," U.S. Patent 7 965 435, Jun. 21, 2011.

[20] R. D. Martin, C. A. Schuetz, D. W. Prather, and T. E. Dillon, "Controlling the phase of optical carriers," U.S. Patent 8 159 737, Apr. 17, 2012.

[21] G. J. Schneider, J. A. Murakowski, C. A. Schuetz, S. Shi, and D. W. Prather, "Radiofrequency signal-generation system with over seven octaves of continuous tuning," *Nature Photon.*, vol. 7, pp. 118–122, Feb. 2013, doi: 10.1038/nphoton.2012.339.

[22] D. W. Prather, G. Schneider, and J. Murakowski, "High spectral-purity carrier wave generation by nonlinear optical mixing," U.S. Patent 8 848 752 B2, Sep. 30, 2014.

[23] J. Macario, P. Yao, S. Shi, A. Zablocki, C. Harrity, R. D. Martin, C. A. Schuetz, and D. W. Prather, "Full spectrum millimeter-wave modulation," *Opt. Exp.*, vol. 20, no. 21, p. 23623, Oct. 2012, doi: 10.1364/OE.20.023623.

[24] A. J. Mercante, S. Shi, P. Yao, L. Xie, R. M. Weikle, and D. W. Prather, "Thin film lithium niobate electro-optic modulator with terahertz operating bandwidth," *Opt. Exp.*, vol. 26, no. 11, p. 14810, May 2018, doi: 10.1364/OE.26.014810.

[25] A. N. R. Ahmed, S. Nelan, S. Shi, P. Yao, A. Mercante, and D. W. Prather, "Subvolt electro-optical modulator on thin-film lithium niobate and silicon nitride hybrid platform," *Opt. Lett.*, vol. 45, no. 5, pp. 1112–1115, May 2020, doi: 10.1364/OL.381892.

[26] S. Nelan, A. Mercante, C. Hurley, S. Shi, P. Yao, B. Shopp, and D. W. Prather, "Compact thin film lithium niobate folded intensity modulator using a waveguide crossing," *Opt. Exp.*, vol. 30, no. 6, pp. 9193–9207, Mar. 2022, doi: 10.1364/OE.453050.

[27] A. Beling, X. Xie, and J. C. Campbell, "High-power, high-linearity photodiodes," *Optica*, vol. 3, no. 3, p. 328, Mar. 2016, doi: 10.1364/OPTICA.3.000328.

[28] T. M. Hancock, S. Gross, J. McSpadden, L. Kushner, J. Milne, J. Hacker, R. Walsh, C. Hornbuckle, C. Campbell, and K. Kobayashi, "The DARPA millimeter wave digital arrays (MIDAS) program," in *Proc. IEEE BiCMOS Compound Semiconductor Integr. Circuits Technol. Symp. (BCICTS)*, Nov. 2020, pp. 1–4, doi: 10.1109/BCICTS48439.2020.9392956.

[29] U. Johannsen, S. Rommel, A. Al-Rawi, D. Konstantinou, T. A. H. Bressner, I. Tafur-Monroy, and A. B. Smolders, "ARoF-fed antenna architectures for 5G networks," in *Proc. Opt. Fiber Commun. Conf. (OFC)*, San Diego, CA, USA, 2019, pp. 1–3, doi: 10.1364/OFC.2019.W1I.3.

[30] *Common Public Radio Interface*. Accessed: Apr. 29, 2022. [Online]. Available: http://www.cpri.info/

[31] S. Shi and D. Prather, "Modular antenna systems and related methods of manufacture," U.S. Patent Appl. 20 210 273 329 A1, Sep. 2, 2021.

[32] S. Galli, R. Menendez, P. Toliver, T. Banwell, J. Jackel, J. Young, and S. Etemad, "Experimental results on the simultaneous transmission of two 2.5 Gbps optical-CDMA channels and a 10 Gbps OOK channel within the same WDM window," in *Proc. OFC/NFOEC Tech. Dig., Opt. Fiber Commun. Conf.*, Mar. 2005, pp. 1–3, doi: 10.1109/OFC.2005.192704.

[33] S. Galli, R. Menendez, P. Toliver, T. Banwell, J. Jackel, J. Young, and S. Etemad, "Novel results on the coexistence of spectrally phase-encoded OCDMA and DWDM," in *Proc. IEEE Int. Conf. Commun.*, May 2005, pp. 1608–1612, doi: 10.1109/ICC.2005.1494615.

[34] G. J. Schneider, J. A. Murakowski, S. Shi, M. Kermalli, S. Galli, X.-F. Qi, and D. W. Prather, "Multiuser-MIMO transmitter based on optical polar-vector modulators," *IEEE Photon. Technol. Lett.*, vol. 30, no. 21, pp. 1834–1837, Nov. 1, 2018, doi: 10.1109/LPT.2018.2868248.

[35] S. Galli, G. J. Schneider, S. Shi, J. A. Murakowski, X.-F. Qi, M. Kermalli, and D. W. Prather, "A novel opto-electronic architecture for large multi-band and multi-beam phased arrays," in *Proc. IEEE Wireless Commun. Netw. Conf. (WCNC)*, Marrakesh, Morocco, Apr. 2019, pp. 1–7, doi: 10.1109/WCNC.2019.8886063.

[36] S. Shi, D. Prather, J. Murakowski, and M. Konkol, "Beam steering antenna transmitter, multi-user antenna MIMO transmitter and related methods of communication," U.S. Patent Appl. 20 220 029 287 A1, Jan. 27, 2022.

[37] S. Galli, M. Kermalli, X.-F. Qi, S. Shi, D. Prather, J. Murakowski, and G. Schneider, "Apparatus and methods for receiving signals using optical lens as a beamformer," U.S. Patent Appl. 20 220 094 374, Mar. 24, 2022.

[38] S. Galli, M. Kermalli, X.-F. Qi, S. Shi, D. Prather, J. Murakowski, and G. Schneider, "Apparatus and methods for transmitting signals using optical lens as a beamformer," U.S. Patent Appl. 20 220 166 137 A1, May 26, 2022.

[39] A. F. Molisch, V. V. Ratnam, S. Han, Z. Li, S. Le Hong Nguyen, L. Li, and K. Haneda, "Hybrid beamforming for massive MIMO: A survey," *IEEE Commun. Mag.*, vol. 55, no. 9, pp. 134–141, Sep. 2017, doi: 10.1109/MCOM.2017.1600400.

[40] A. Adhikary, J. Nam, J.-Y. Ahn, and G. Caire, "Joint spatial division and multiplexing—The large-scale array regime," *IEEE Trans. Inf. Theory*, vol. 59, no. 10, pp. 6441–6463, Oct. 2013, doi: 10.1109/TIT.2013.2269476.

[41] J. Brady, N. Behdad, and A. M. Sayeed, "Beamspace MIMO for millimeter-wave communications: System architecture, modeling, analysis, and measurements," *IEEE Trans. Antennas Propag.*, vol. 61, no. 7, pp. 3814–3827, Jul. 2013, doi: 10.1109/TAP.2013.2254442.

[42] P. S. Hall and S. J. Vetterlein, "Review of radio frequency beamforming techniques for scanned and multiple beam antennas," *IEE Proc. H-Microw., Antennas Propag.*, vol. 137, pp. 293–303, Oct. 1990, doi: 10.1049/ip-h-2.1990.0055.

[43] M. A. B. Abbasi, V. F. Fusco, H. Tataria, and M. Matthaiou, "Lens–based beamformer for low–complexity millimeter–wave cellular systems," in *Proc. ESA Workshop Millimetre-Wave Technol. Appl.*, Noordwijk, The Netherlands, Dec. 2018.

[44] D. Solomon. (Mar. 17, 2015). *AT&T Brought a Giant Eyeball to SXSW to Double Cell Capacity*. Fast Company. Accessed: Nov. 17, 2022. [Online]. Available: https://www.fastcompany.com/3043818/att-brought-a-giant-eyeball-to-sxsw-to-double-cell-capacity

[45] Z. Shen, B. Jin, J. Zhao, Y. Feng, L. Kang, W. Xu, J. Chen, and P. Wu, "Design of transmission-type coding metasurface and its application of beam forming," *Appl. Phys. Lett.*, vol. 109, no. 12, Sep. 2016, Art. no. 121103, doi: 10.1063/1.4962947.

[46] M. Jiang, Z. N. Chen, Y. Zhang, W. Hong, and X. Xuan, "Metamaterial-based thin planar lens antenna for spatial beamforming and multi-beam massive MIMO," *IEEE Trans. Antennas Propag.*, vol. 65, no. 2, pp. 464–472, Feb. 2017, doi: 10.1109/TAP.2016.2631589.

[47] Z. N. Chen, T. Li, and W. E. I. Liu, "Microwave metasurface-based lens antennas for 5G and beyond," in *Proc. 14th Eur. Conf. Antennas Propag. (EuCAP)*, Mar. 2020, pp. 1–4, doi: 10.23919/EuCAP48036.2020.9135285.

[48] L. Stefanini, A. Rech, D. Ramaccia, S. Tomasin, A. Toscano, F. Moretto, and F. Bilotti, "Multibeam scanning antenna system based on beamforming metasurface for fast 5G NR initial access," *IEEE Access*, vol. 10, pp. 65982–65995, 2022, doi: 10.1109/ACCESS.2022.3183754.

[49] L. Stefanini, D. Ramaccia, F. Bilotti, and A. Toscano, "Gradient metasurface dome implements a matrix beamforming network for 2D antenna arrays," in *Proc. IEEE Int. Symp. Antennas Propag. USNC-URSI Radio Sci. Meeting (APS/URSI)*, Dec. 2021, pp. 775–776, doi: 10.1109/APS/URSI47566.2021.9703914.

[50] J. W. Goodman, *Introduction to Fourier Optics*, 4th ed. New York, NY, USA: W. H. Freeman, 2017.

[51] D. D. Ross, M. R. Konkol, S. Shi, and D. W. Prather, "Photodiode-integrated UWB phased array antennas," in *Proc. IEEE Photon. Conf. (IPC)*, Orlando, FL, USA, Oct. 2017, pp. 109–110, doi: 10.1109/IPCon.2017.8116026.

[52] J. G. Burnett and J. D. C. Jones, "Cutting optical fibers to equal lengths for broadband stellar interferometry," *Appl. Opt.*, vol. 31, no. 16, p. 2977, Jun. 1992, doi: 10.1364/AO.31.002977.

[53] D. W. Prather, S. Shi, G. J. Schneider, P. Yao, C. Schuetz, J. Murakowski, J. C. Deroba, F. Wang, M. R. Konkol, and D. D. Ross, "Optically upconverted, spatially coherent phased-array-antenna feed networks for beam-space MIMO in 5G cellular communications," *IEEE Trans. Antennas Propag.*, vol. 65, no. 12, pp. 6432–6443, Dec. 2017, doi: 10.1109/TAP.2017.2735549.

[54] G. Schneider, C. Schuetz, J. Murakowski, T. Dillon, S. Shi, and D. Prather, "Phased-array radio frequency receiver and methods of operation," U.S. Patent Appl. 20 190 372 219 A1, Dec. 5, 2019.

[55] D. Jorgesen. (2018). *IQ, Image Reject, and Single Sideband Mixer Primer*. Marki Microwave, Inc. [Online]. Available: https://www.markimicrowave.com/assets/appnotes/IQ_IR_SSB_Mixer_Primer.pdf

[56] B. C. Henderson and J. A. Cook, "Image-reject and single-sideband mixers," Watkins-Johnson, Palo Alto, CA, USA, Tech. Rep., 12, Jun. 1985.

[57] D. Zhu and S. Pan, "Photonics-based microwave image-reject mixer," *Photonics*, vol. 5, no. 2, p. 6, Mar. 2018, doi: 10.3390/photonics5020006.

[58] G. Schneider and J. Murakowski, "Photonic image rejection RF mixer, a phased-array radio frequency receiver implementing the same and related methods of operation," U.S. Patent Appl. 17/703 916, Mar. 24, 2022.

[59] S. Won and S. W. Choi, "A tutorial on 3GPP initial cell search: Exploring a potential for intelligence based cell search," *IEEE Access*, vol. 9, pp. 100223–100263, 2021, doi: 10.1109/ACCESS.2021.3095346.

[60] J. C. Deroba, G. J. Schneider, C. A. Schuetz, and D. W. Prather, "Smart antenna using element-level photonic up-conversion to generate an apodized beam-space for increased spatial isolation," *IEEE Antennas Wireless Propag. Lett.*, vol. 16, pp. 2274–2277, 2017, doi: 10.1109/LAWP.2017.2714099.

[61] J. C. Deroba, G. J. Schneider, C. A. Schuetz, and D. W. Prather, "Tapered multi-beam arrays via an optically power-efficient photonic architecture," *J. Lightw. Technol.*, vol. 36, no. 11, pp. 2259–2270, Jun. 1, 2018, doi: 10.1109/JLT.2018.2805868.

[62] J. C. Deroba, G. J. Schneider, C. A. Schuetz, and D. W. Prather, "Multifunction radio frequency photonic array with beam-space down-converting receiver," *IEEE Trans. Aerosp. Electron. Syst.*, vol. 54, no. 6, pp. 2746–2761, Dec. 2018, doi: 10.1109/TAES.2018.2829359.

[63] P. K. Saha. (Apr. 2022). *A Quantitative Analysis of the Power Advantage of Hybrid Beamforming for Multibeam Phased Array Receivers*. Accessed: Nov. 28, 2022. Analog Devices, Inc. [Online]. Available: https://www.analog.com/en/technical-articles/power-advantage-of-hybrid-beamforming.html

[64] D. Prather, G. J. Schneider, S. Shi, J. A. Murakowski, C. Schuetz, and T. Creazzo, "Multifunctional, high beam-bandwidth product phased array system," presented at the GOMACTech Conf., Miami, FL, USA, Mar. 21–24, 2022, Paper P9.61.

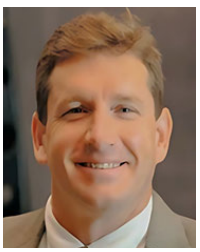

DENNIS W. PRATHER (Fellow, IEEE) received the B.S.E.E., M.S.E.E., and Ph.D. degrees from the University of Maryland, in 1989, 1993, and 1997, respectively. Began his professional career by joining the U.S. Navy, in 1982 as an E-1, where he served until 2021, and retired at the rank of CAPT (O-6) as an Engineering Duty Officer. He worked as a Senior Research Engineer at the Army Research Laboratory, where he performed research on both optical devices and architectures for information processing. In 1997, he joined the Department of Electrical and Computer Engineering, University of Delaware, where he is currently the College of Engineering Alumni Distinguished Professor. He is also an Endowed Professor of electrical engineering. His research interests include theoretical and experimental aspects of RF-photonic elements and their integration into various systems for imaging, communications, and radar. He is a fellow of the National Academy of Inventors (NAI), the Society of Photo-Instrumentation Engineers (SPIE), and the Optica (formerly Optical Society of America (OSA)).

STEFANO GALLI (Fellow, IEEE) received the Ph.D. degree in electrical engineering from the University of Rome (Italy). Since 2021, he has been a Chief Scientist and a Senior Manager at the Wireless and Optical Department, Peraton Inc., NJ, USA. His past positions include various technical leadership positions at Futurewei Technologies, ASSIA, Panasonic, Bellcore; and consulting roles for ERDF and STR. He has been active in standardization, submitting to a variety of Standards Developing Organizations numerous contributions on power line communications, smart grid communications, xDSL/G.fast, and network function virtualization. He has also served as the ITU-T SG15/Q15 Rapporteur for the ''Smart Grid Communications'' Group. He is the co-inventor of 29 issued/pending patents, the co-author of more than 100 papers, one book, and five book chapters. He is active in IEEE, where he is currently serving as a PSPB Member-at-Large and Treasurer (2021–2022). He was a co-recipient of the three IEEE Best Paper Awards (including the 2013 IEEE Donald G. Fink Best Paper Award), the 2014 Broadband Forum Outstanding Contributor Award, and various technical and service ComSoc recognitions. He has served in the IEEE Fellow Committee as the Chair (2018–2019), the Vice Chair (2016–2017), and a member (2013–2015). He is also active in the Communications Society (ComSoc), where he was elected to the Board of Governors as the Vice-President of Technical and Educational Activities (2021); the Vice-President or Industry and Standards (2018–2019); the Member-at-Large (2008–2013).

GARRETT J. SCHNEIDER received the B.S. degree in astronomy and physics from Haverford College, Haverford, PA, USA, in 1993, and the Ph.D. degree in physics from the University of Delaware, Newark, DE, USA, in 2002. Since 2002, he has been with the Department of Electrical and Computer Engineering, University of Delaware, where he is currently an Assistant Research Professor. He is also a Consulting Engineer with Phase Sensitive Innovations, Inc., Newark. He is the coauthor of more than 100 peer-reviewed journals and conference publications, and several books/book chapters, and has 12 issued patents, in the fields of nanofabrication and RF photonic system design. His areas of expertise include nonlinear optics, microwave photonics, optical and RF device, system characterization techniques, and nanofabrication. His current research interests include RF/microwave/millimeter-wave photonics for applications in telecommunications and remote sensing.

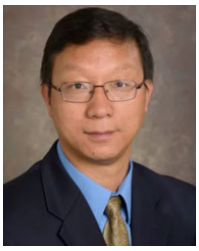

SHOUYUAN SHI received the B.S., M.S., and Ph.D. degrees from Xidian University, Xi'an, China, in 1991, 1994, and 1997, respectively, all in electrical engineering. He is currently a Research Professor with the Department of Electrical and Computer Engineering, University of Delaware, Newark, DE, USA. He is also a Consulting Engineer with Phase Sensitive Innovations, Inc., Newark. He is the author or the coauthor of eight books and book chapters, and more than 380 peer-reviewed journals and conference publications. He holds over 20 issued U.S. patents. His research interests include computational electromagnetics, micro-optics and nano-photonics, and RF-photonics technologies and applications, including ultra-wideband RF antennas, optically addressed phase arrays, ultra-wideband electro-optic devices and systems, and passive and active millimeter wave imaging systems. He is an active reviewer of more than 20 international peer-reviewed journals in the research areas of optics and photonics, RF, electro-optics, and electromagnetics. He is also served as the Topic Editor of *Photonic Devices and Materials* and the *Optical and Photonic Letters* and the Editorial Board Member of *Advanced Optics*.

JANUSZ A. MURAKOWSKI (Member, IEEE) received the M.S. degrees in physics from the Imperial College, London, U.K., in 1991 and A. Mickiewicz University, Poznan, Poland, in 1990, and the Ph.D. degree in physics from the University of Delaware, USA, in 1999. He currently holds the position of a Senior Scientist at Phase Sensitive Innovations, Inc., Newark, DE, USA. Until 2022, he was also an Associate Research Professor at the Department of Electrical and Computer Engineering, University of Delaware. He holds 31 issued U.S. patents. He is the author or the coauthor of several books and book chapters, and more than a 100 of peer-reviewed journals and conference publications. His areas of expertise include electromagnetic science and engineering, micro- and nano-fabrication, photonic and electro-optic system design, innovation in addition to photonic modeling, design, fabrication, and characterization. His current research interests include RF/microwave photonics, including system design, electro-optic modulation, nonlinear optical processes, transmission, detection, and imaging.

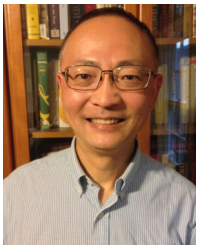

XIAO-FENG QI (Senior Member, IEEE) received the Ph.D. degree from the University of Connecticut, in 1992. He was the Senior Director of Radio Algorithms Research, Futurewei Technologies, Inc., from 2014 to 2021, where he oversaw the 5G/6G research portfolio of wireless communication and sensing technologies. From 1992 to 2014, he was with AT&T Microelectronics, Globespan Semiconductors, Level One Communications, Intel, and Broadcom, where he took on a Lead Designer and a Supervisory roles in wireline and wireless product research and development. He was a Senior Director of advanced research at Intel and a Technical Manager of Systems Group at Broadcom. He is currently a Professor at the Electrical and Computer Engineering Department, University of Delaware, and the Chief Strategy Officer, Phase Sensitive Innovations, Inc. He is the (co)author of more than 20 granted U.S. and international patents and a dozen refereed journals and conference publications. His current research interest includes statistical signal processing techniques applied to wireless communications and sensing.

CHRISTOPHER SCHUETZ received the B.S. degree in electrical engineering from Virginia Polytechnic and State University, in 1997, and the M.S. and Ph.D. degrees in millimeter-wave imaging from the Graduate School, University of Delaware, in 2004 and 2007, respectively. Since graduating with honors, he has worked with companies, such as BAE Systems and Optical Crosslinks, Inc., where his research interests include microwave photonics and polymer optical waveguides. After completing his doctorate, he has cofounded Phase Sensitive Innovations, Inc., with his advisor Dr. Dennis Prather, where he has served as a CTO, since its founding. He served a dual appointment with the University of Delaware, from 2012 to 2015, where he developed techniques for multifunctional receive and transmit phased arrays based on RF photonics. His expertise is in the area of mmW imaging, phenomenology, and detection and RF photonic processing techniques, where he has authored or coauthored over 100 papers and holds over 15 patents in this field. He was a recipient of the AFOSR Young Investigator Grant. In 2015, he returned full time to PSI, but retained an affiliated faculty appointment at UD. He has served on the conference committee for the SPIE Passive Millimeter Wave Imaging Technology Conference. He was the Co-Chair of SPIE Photonics West Session on RF and mmW Photonics. He served as the Co-Editor for a Special Issue on *Applied Optics on RF Imaging*.